IRAQI JOURNAL OF APPLIED PHYSICS

The *Iraqi Journal of Applied Physics (IJAP)* is a peer reviewed journal of high quality devoted to the publication of original research papers from applied physics and their broad range of applications. IJAP publishes quality original research papers, comprehensive review articles, survey articles, book reviews, dissertation abstracts in physics and its applications in the broadest sense. It is intended that the journal may act as an interdisciplinary forum for Physics and its applications. Innovative applications and material that brings together diverse areas of Physics are particularly welcome. Review articles in selected areas are published from time to time. It aims to disseminate knowledge; provide a learned reference in the field; and establish channels of communication between academic and research experts, policy makers and executives in industry, commerce and investment institutions. IJAP is a quarterly specialized periodical dedicated to publishing original papers, letters and reviews in: Applied & Nonlinear Optics, Applied Mechanics & Thermodynamics, Digital & Optical Communications, Electronic Materials & Devices, Laser Physics & Applications, Plasma Physics & Applications, Quantum Physics & Spectroscopy, Semiconductors & Optoelectronics, Solid State Physics & Applications, Alternative and Renewable Energy, and Computers and Networks.

ISSN (Print): 1813-2065, ISSN (Online): 2309-1673, ISSN (Letters): 1999-656X

EDITORIAL BOARD

Raad A. KHAMIS	Asst. Professor	Editor-in-Chief	Plasma Physics	IRAQ
Walid K. HAMOUDI	Professor	Member	Laser Physics	IRAQ
Dayah N. RAOUF	Asst. Professor	Member	Laser and Optics	IRAQ
Raid A. ISMAIL	Professor	Member	Semiconductor Physics	IRAQ
Oday A. HAMMADI	Asst. Professor	Managing Editor	Molecular Physics	IRAQ
Intesar F. RAMLEY	Professor	Member	Communications Eng.	CANADA
Khaled A. AHMED	Professor	Member	Theoretical Physics	IRAQ
Manal J. AL-KINDY	Asst. Professor	Member	Electrical Engineering	IRAQ
Kais A. AL-NAIMEE	Asst. Professor	Member	Quantum Optics	ITALY
Abdulhadi ALKHALILI	Professor	Member	Medical Physics	U.S.A
Abdulmajeed IBRAHIM	Professor	Member	Solid State Physics	IRAQ
Loay E. GEORGE	Asst. Professor	Member	Computers & Networks	IRAQ
Haitham M. MIKHLIF	Lecturer	Member	Molecular Physics	UK

Editorial Office:
P. O. Box 55259, Baghdad 12001, IRAQ
Website: www.iraqiphysicsjournal.com
Emails: info@iraqiphysicsjournal.com, editor_ijap@yahoo.co.uk, editor@ijaponline.com

ADVISORY BOARD

Abdullah M. SUHAIL, Professor, Department of Physics, College of Science, University of Baghdad, IRAQ
Adel K. HAMOUDI, Professor, Department of Physics, College of Science, University of Baghdad, IRAQ
Andrei KASIMOV, Professor, Institute of Material Science, National Academy of Science of Ukraine, Kiev, UKRAINE
Ashok KUMAR, Professor, Harcourt Butler Technological Institute, Nawabganj, Kanpur, Uttar Pradesh 208 002, INDIA
Chang Hee NAM, Professor, Korean Advanced Institute of Science and Technology, 291 Daehak-ro, Daejeon, KOREA
El-Sayed M. FARAG, Professor, Department of Sciences, College of Engineering, Al-Minofiya University, EGYPT
Franko KUEPPERS, Professor, Darmstadt University of Technology, Mornewegstraße 32, Darmstadt, GERMANY
Gang XU, Assistant Professor, Department of Engineering and Physics, University of Central Oklahoma, U.S.A
Heidi ABRAHAMSE, Professor, Faculty of Health Sciences, University of Johannesburg, SOUTH AFRICA
Mansoor SHEIK-BAHAE, Associate Professor, Department of Physics & Astronomy, University of New Mexico, U.S.A
Mazin M. ELIAS, Professor, Laser Institute for Postgraduates, University of Baghdad, Al-Jadiriyah, Baghdad, IRAQ
Mohammad Robi HOSSAN, Assistant Professor, Dept. of Engineering and Physics, Univ. of Central Oklahoma, U.S.A
Mohammed A. HABEEB, Professor, Department of Physics, Faculty of Science, Al-Nahrain University, Baghdad, IRAQ
Morshed KHANDAKER, Associate Professor, Dept. of Engineering and Physics, Univ. of Central Oklahoma, U.S.A
Muhammad A. HUSSAIN, Assistant Professor, Dept. of Laser and Optoelectronics Eng., Al-Nahrain University, IRAQ
Mutaz S. ABDUL-WAHAB, Assistant Professor, Dept. of Electric and Electronic Eng., University of Technology, IRAQ
Nadir F. HABOUBI, Professor, Department of Physics, College of Education, Al-Mustansiriya Univ., Baghdad, IRAQ
Shivaji H. PAWAR, Professor, D.Y. Patil University, Kasaba Bawada, Kolhapur-416 006, INDIA
Xueming LIU, Professor, Department of Electronic Engineering, Tsinghua University, Shuang Qing Lu, Beijing, CHINA
Yanko SAROV, Assistant Professor, Micro- and Nanoelectronic Systems, Technical University Ilmenau, GERMANY
Yushihiro TAGUCHI, Professor, Department of Physics, Chuo University, Higashinakano Hachioji-shi, Tokyo, JAPAN

SPONSORED AND PUBLISHED BY
THE IRAQI SOCIETY FOR ALTERNATIVE AND RENEWABLE ENERGY SOURCES & TECHNIQUES (I.S.A.R.E.S.T.)

IRAQI JOURNAL OF APPLIED PHYSICS

ISSN (Print): 1813-2065, ISSN (Online): 2309-1673, ISSN (Letters): 1999-656X

" INSTRUCTIONS TO AUTHORS "

CONTRIBUTIONS

Contributions to be published in this journal should be original research works, i.e., those not already published or submitted for publication elsewhere, individual papers or letters to editor.

Manuscripts should be submitted to the editor at the mailing address:

Iraqi Journal of Applied Physics, Editorial Board, P. O. Box 55259, Baghdad 12001, IRAQ
Website: www.iraqiphysicsjournal.com
Email: editor@iraqiphysicsjournal.com, editor_ijap@yahoo.co.uk

MANUSCRIPTS

Two hard copies with soft copy on a compact disc (CD) should be submitted to Editor in the following configuration:

- **One-column** Double-spaced one-side A4 size with 2.5 cm margins of all sides
- Times New Roman font (16pt bold for title, 14pt bold for names, 12pt bold for headings, 12pt regular for text)
- Letters should not exceed 10 pages, papers should not exceed 20 pages and reviews are up to author.
- Manuscripts presented in English only are accepted.
- English abstract not exceed 150 words
- 4 keywords (at least) should be maintained on (PACS preferred)
- Author(s) should express all quantities in SI units
- Equations should be written in equation form (*italic* and symbolic)
- Figures and Tables should be separated from text
- Figures and diagrams can be submitted in colors for assessment and they will be returned to authors after provide printable copies
- Charts should be indicated by the software used for
- Only original or high-resolution scanner photos are accepted
- For electronic submission, articles should be formatted with MS-Word software.

AUTHOR NAMES AND AFFILIATIONS

It is IJAP policy that all those who have participated significantly in the technical aspects of a paper be recognized as co-authors or cited in the acknowledgments. In the case of a paper with more than one author, correspondence concerning the paper will be sent to the first author unless staff is advised otherwise.

Author name should consist of first name, middle initial, last name. The author affiliation should consist of the following, as applicable, in the order noted:

- Company or college (with department name or company division), Postal address, City, state, zip code, Country name, contacting telephone, and e-mail

REFERENCES

The references should be brought at the end of the article, and numbered in the order of their appearance in the paper. The reference list should be cited in accordance with the following examples:

[1] X. Ning and M.R. Lovell, "On the Sliding Friction Characteristics of Unidirectional Continuous FRP Composites", *ASME J. Tribol.*, 124(1) (2002) 5-13.

[2] M. Barnes, "Stresses in Solenoids", *J. Appl. Phys.*, 48(5) (2001) 2000–2008.

[3] J. Jones, **"Contact Mechanics"**, Cambridge University Press (Cambridge, UK) (2000), Ch.6, p.56.

[4] Y. Lee, S.A. Korpela and R. Horne, "Structure of Multi-Cellular Natural Convection in a Tall Vertical Annulus", Proc. 7th International Heat Transfer Conference, U. Grigul et al., eds., Hemisphere (Washington DC), 2 (1982) 221–226.

[5] M. Hashish, "Waterjet Technology Development", High Pressure Technology, PVP-Vol. 406 (2000) 135-140.

[6] D.W. Watson, "Thermodynamic Analysis", ASME Paper No. 97-GT-288 (1997).

[7] C.Y. Tung, "Evaporative Heat Transfer in the Contact Line of a Mixture", Ph.D. thesis, Rensselaer Polytechnic Institute, Troy, NY (1982).

PROOFS

Authors will receive proofs of papers and are requested to return one corrected hard copy with a WORD copy on a compact disc (CD). New materials inserted in the original text without Editor permission may cause rejection of paper.

COPYRIGHT FORM

Author(s) will be asked to transfer copyrights of the article to the Journal soon after acceptance of it. This will ensure the widest possible dissemination of information.

OFFPRINTS

Authors will receive offprints free of charge and any additional reprints can be ordered.

SUBSCRIPTION AND ORDERS

Annual fees (4 issues per year) of subscription are:

50 US$ for individuals inside Iraq;	**200** US$ for institutions inside Iraq;
100 US$ for individuals abroad;	**300** US$ for institutions abroad.

Fees are reduced by 25% for I.S.A.R.E.S.T. members. Orders of issues can be submitted by contacting the editor-in-chief or editorial office at admin@iraqiphysicsjournal.com, or editor_ijap@yahoo.co.uk to maintain the address of issue delivery and payment way.

IRAQI JOURNAL OF APPLIED PHYSICS
Vol. 17, No. 1, January-March 2021, pp. 3-8

Preparation and Characterization of Ni-doped TiO_2 Nanostructures for Surface Cleaning Applications

Ruqia A.H. Hassan
Fuad T. Ibrahim

*Department of Physics,
College of Science,
Baghdad University,
Baghdad, IRAQ*

In this work, pure and Ni-doped nanostructured titanium dioxide (TiO_2) thin films were prepared by dc reactive magnetron sputtering technique onto glass substrates. The structural characteristics of these nanostructures were determined and analyzed. Scanning electron microscopy (SEM) confirmed the formation of smooth and well-dispersed surfaces. The optical measurements in the spectral range 300-800 nm have confirmed that the optical energy gap of the pure and Ni-doped TiO_2 prepared films were 3.3 and 2.95 eV, respectively. The contact angle measurements were carried out under air setting using the sessile drop method. The measured values of the contact angle of a water droplet on the surface before and after irradiation with UV light for 15 and 30 minutes show that the contact angle of a water droplet on the pure and Ni-doped TiO_2 surfaces was decreased after 30 minutes of irradiated and the prepared samples show high hydrophilicity.

Keywords: Photocatalysis; Titanium dioxide; Surface cleaning; Nanostructures
Received: 18 December 2020; **Revised**: 24 January 2021; **Accepted**: 31 January 2021

1. Introduction

The development of semi-conductors able to use visible light has been a field of growing interest during the last years [1]. Among various oxide and non-oxide semiconductor photocatalysts, titanium dioxide (TiO_2) has been proven to be the most suitable for wide environmental and energy applications [2], because of its non-toxicity, photochemical stability, low cost [3], and high photocatalytic activity with a band gap of 3.2 eV [4].

Titanium dioxide has three phases in nature, rutile, anatase, and brookite [5]. Rutile is the only stable phase, whereas anatase and brookite e are metastable at all temperatures and transfer to rutile when they are heated [6]. The anatase is generally reported to show the highest photoactivity compared to the brookite or rutile because of the low recombination rate of its photogenerated electrons and holes [7].

Titanium dioxide (TiO_2) has been used widely in various fields, such as solar cells, photocatalytic splitting of water for green-energy hydrogen (H_2) production, air and water purification by removal of organic and inorganic pollutants, super-hydrophilicity for antifogging and self-cleaning, and photo-killing of pathogenic bacteria [8].

The self-cleaning property of TiO_2 thin films has become an interesting subject in recent years [9]. The self-cleaning property has been known to be a combined effect of the two photoactive characteristic properties of TiO_2 thin films: super-hydrophilicity and photocatalysis. The photocatalytic property helps decompose the organic compounds that come into contact with the surface and thus prevents them from building up. The super-hydrophilic property of the TiO_2 film on the surface allows water to spread completely across the surface rather than remain as droplets, thus making the surface easy to wash. Thus, the photocatalytic and hydrophilic properties of TiO_2 coated glass allow the water to easier wash away deposited particles [10]. By increasing the hydrophilicity and wettability characteristics of a surface, which depends on surface microstructure, surface chemical composition and surface geometry, water can spread better over the surface and improve the cleaning character of the surface. Many attempts are made to increase the hydrophilicity of TiO_2 thin films. It seems that the hydrophilicity can be improved by doping TiO_2 [11]. Also, TiO_2 films show higher hydrophilicity properties and photocatalytic activities under UV irradiation [12].

Different deposition techniques can be used to form titanium oxides films, including plasma-enhanced chemical vapor deposition (PECVD) [13], hydrothermal method [14] , spray pyrolysis [15], sol-gel method [16], electron beam evaporation (EBE) [17], pulsed-laser deposition (PLD) technique [18], and reactive dc magnetron sputtering [19].

In this study, pure and Ni-doped nanostructured TiO_2 thin films were prepared by dc reactive magnetron sputtering technique. The spectral and structural characteristics of these thin films were determined and studied. The prepared samples can be used as self-cleaning surfaces.

2. Experimental Work

A dc reactive magnetron sputtering system shown in Fig. (1) was used in this work. The chamber was evacuated by a Leybold-Heraeus two-stage rotary pump (24 m^3/h) to a base pressure of about $5x10^{-3}$ mbar. A solid titanium sheet (99.99% purity) was used as a target. The chamber was filled with highly-pure gas mixture containing argon and oxygen to the desired pressure (0.25 mbar). The mixing ratio could be precisely varied by mixing the two gases in an external mixer before pumped into the deposition chamber. The optimum mixing ratio was 1:1. The titanium dioxide thin films were deposited onto glass substrates after different deposition times. However, the results presented herein are belonging to the samples prepared after deposition time of 2 hours.

In order to perform doping process on the prepared TiO_2 samples, a highly-pure (99.99%) nickel sheet with ring shape of 4cm outer diameter and 2cm inner diameter was placed on the cathode surface as in the configuration shown in Fig. (2). In this case, the gas mixture was containing argon only in order to avoid the formation of nickel oxide.

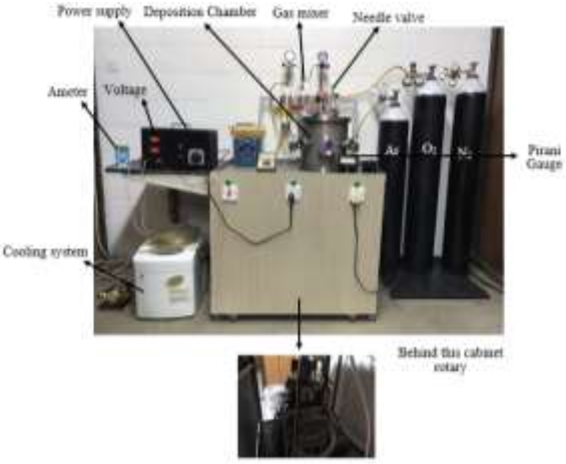

Fig. (1) The dc reactive magnetron sputtering system used in the present work

Hydrophilic behavior was evaluated by measuring the contact angle of a water droplet on the films using a contact angle device shown in Fig. (3). A water droplet is injected on the surface of the film using a micro-injector (5µl) syringe pointed vertically down onto the sample surface. High-resolution camera with a macro lens which captures the image of the water droplet. These images are analyzed using analysis software. The contact angle of the water droplets was measured on the surfaces of TiO_2 samples (pure and doped) before and after irradiation with a UV source.

Fig. (2) Geometrical arrangement of the co-sputtering configuration using Ti and Ni targets

Fig. (3) Experimental setup of contact angle measurement

3. Results and Discussion

The crystalline structure of the samples prepared after deposition time of 2 hours was investigated by the x-ray diffraction (XRD) patterns as shown in Fig. (4). Both anatase (A) and rutile (R) phases of TiO_2 were observed in these patterns. The diffraction peaks at 2θ values of 48.1°, 53.9°, 55.1° and 68.9° are corresponding to (200), (105), (211) and (116) crystal planes, respectively. They confirm the formation of anatase (A) phase according to the JCPDS 21-1272 [20]. The rutile (R) phase was confirmed by the diffraction peaks assigned at 27.8°, 36.2° and 62.7 corresponding to (110), (101) and (002) crystal planes, respectively according to the JCPDS 21-1276 [21].

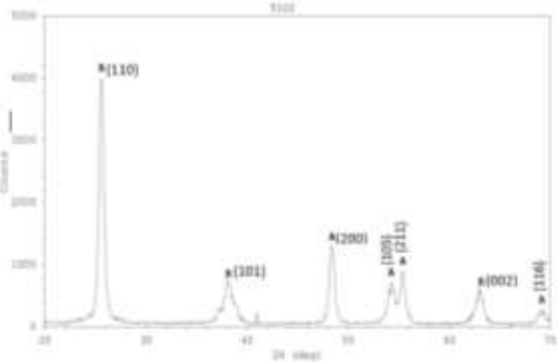

Fig. (4) XRD pattern for mixed-phase (anatase/rutile) TiO_2 samples prepared using gas mixing ratio of 1:1 after deposition time of 2 hours

Figure (5) shows the XRD pattern of Ni-doped TiO_2 thin films prepared using $Ar:O_2$ gas mixture of 1:1 after deposition time of 2 hours. The diffraction pattern reveals the formation of mixed-phase (anatase/rutile) TiO_2 structures as all diffraction peaks assigned, The diffraction peaks at 2θ values of at 25.2°, 37.8°, 49°, 53.9°, 62.8°, 68.9°, and 75.55° are corresponding to (101), (004), (200), (105), (118), (116), and (125) crystal planes, respectively. They confirm the formation of the anatase (A) phase according to the JCPDS 21-1272 [20]. The rutile (R) phase was confirmed by the diffraction peaks assigned at 27.8°, 41.5°, and 54.9° corresponding to crystal planes of (110), (111), and (211), respectively according to the JCPDS 88-1175 [22]. The diffraction peaks at 44.6°, 52°, and 76.9° are corresponding to (111), (200), and (220) crystal planes, respectively, those belonging to Ni dopants according to the JCPDS 1-1260 [23].

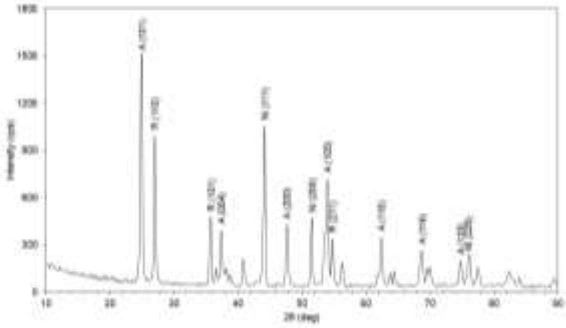

Fig. (5) XRD pattern for Ni-doped TiO_2 sample prepared using gas mixing ratio of 1:1 after deposition time of 2 hours

Figure (6) shows the Fourier-transform infrared (FTIR) spectrum of the sample prepared using $Ar:O_2$ gas mixing ratio of 1:1 after deposition time of 2 hours. This spectrum was recorded in the wavenumber range 400-4000 cm^{-1} using Shimadzu 8400S FTIR spectrometer. The band assigned to Ti-O stretching vibration was observed at around 447 and 667 cm^{-1} while the peak at 408.91 cm^{-1} is due to Ti-O-Ti bonds in the TiO_2 lattice [24]. The absorption band at 1620 cm^{-1} is due to the presence of O–H bending vibration [25], which is probably because of the re-absorption of water from the atmosphere. The absorption bands around 3450 cm^{-1} are attributed to the presence of the O–H stretching mode [26,27]. The FTIR spectrum confirms the absence of any impurities in the prepared samples. This can be attributed to the operation and preparation at the optimum conditions, which represents one of the most important advantages of the magnetron sputtering technique.

The absorption spectra of mixed-phase undoped and Ni-doped TiO_2 films were recorded in the spectral range of 300-800 nm. Figure (7) shows the absorption spectrum of the mixed-phase (anatase-rutile) TiO_2 nanostructures prepared using gas mixing ratio of 1:1 after deposition time of 2 hours. We observed that the absorbance value decreases with increasing wavelength until it almost constant. The absorbance decreases slightly in the region of low energies (long wavelengths) while it increases drastically in the region of high energies (short wavelengths). This means that the absorbance was high in the ultraviolet region, then it gradually decreased in the visible region, and then there is almost no absorption in the infrared region. The absorption edge was at 375.7 nm.

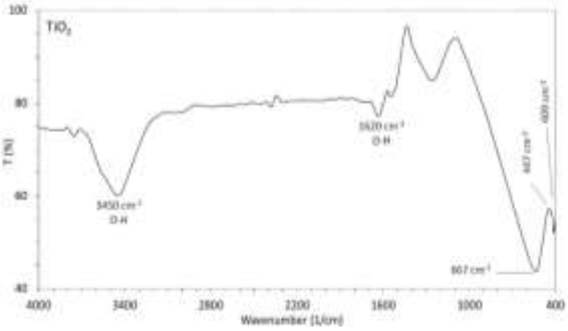

Fig. (6) FTIR spectrum of undoped TiO_2 sample prepared at inter-electrode distance of 4 cm and using $Ar:O_2$ gas mixture of 1:1 after deposition time of 2 hour

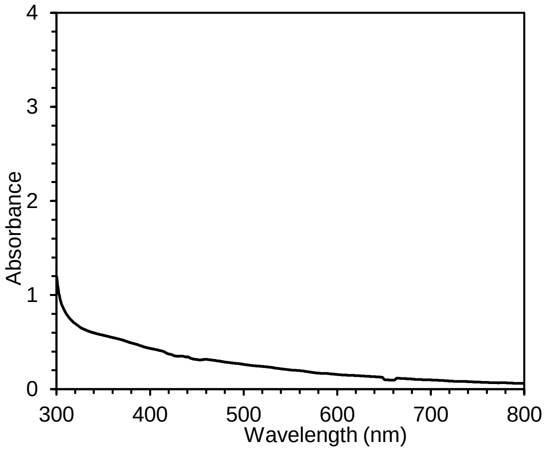

Fig. (8) Absorption spectrum of undoped TiO_2 sample prepared using $Ar:O_2$ gas mixture 1:1 after deposition time 2 hours

The absorption spectrum of Ni-doped TiO_2 thin films is shown in Fig. (8). The Ni dopants have successfully shifted the absorption of TiO_2 from UV to the visible region because they tend to accept more electrons and facilitate more holes to transport at the surface. The absorption edge was at 420 nm.

The doping process of TiO_2 nanostructures with Ni ions contributes to the modification of the photocatalyst material throughout working in a spectral region of longer wavelengths, i.e., from UV to visible regions. The energy band gap (E_g) was reduced from 3.3 to 2.95 eV in case of Ni-doped TiO_2 films, as shown in Fig. (9).

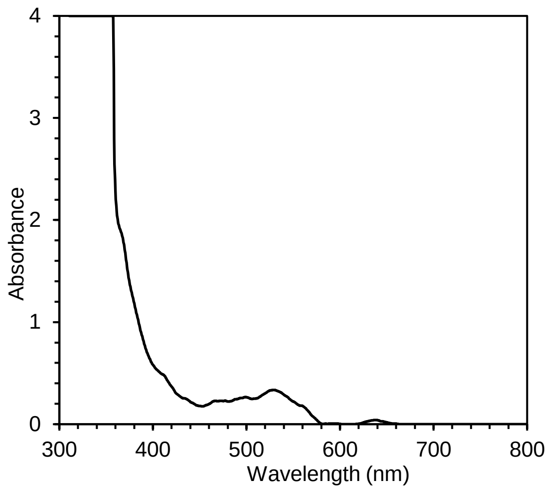

Fig. (8) Absorption spectrum of Ni-doped TiO_2 sample prepared using $Ar{:}O_2$ gas mixture 1:1 after deposition time 2 hours

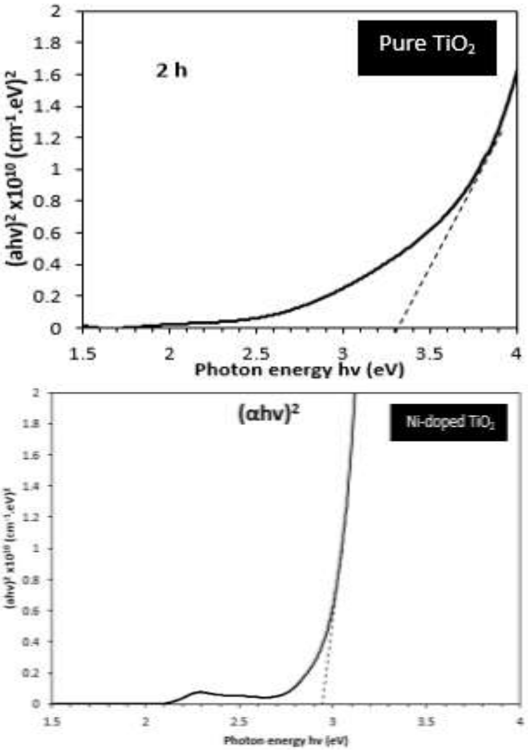

Fig. (9) Determination of energy band gap for undoped and Ni-doped TiO_2 samples prepared in this work

Table (1) Results of the film thickness and energy band gap of undoped and Ni-doped TiO_2 thin films

Sample	Thickness (nm)	Energy gap (eV)
Pure TiO_2	190	3.3
Ni-doped TiO_2	204	2.95

Figure (10) shows the surface morphology of TiO_2 film grown on glass substrates with three different scales (200nm, 500nm and 1μm) of scanning electron microscopy (SEM). The prepared surface is smooth and uniform. The nanoparticles are aligned and homogeneously distributed (with no voids), but their diameters and lengths are rather uniform. The surface also contains polyhedral shells distributed dispersively on the substrate, with some of them lineup along the nanoparticle. The SEM images show small granular grains distributed throughout the surface without any cracks. Also, spherical grains of sizes equal to 60-80 nm are also observed.

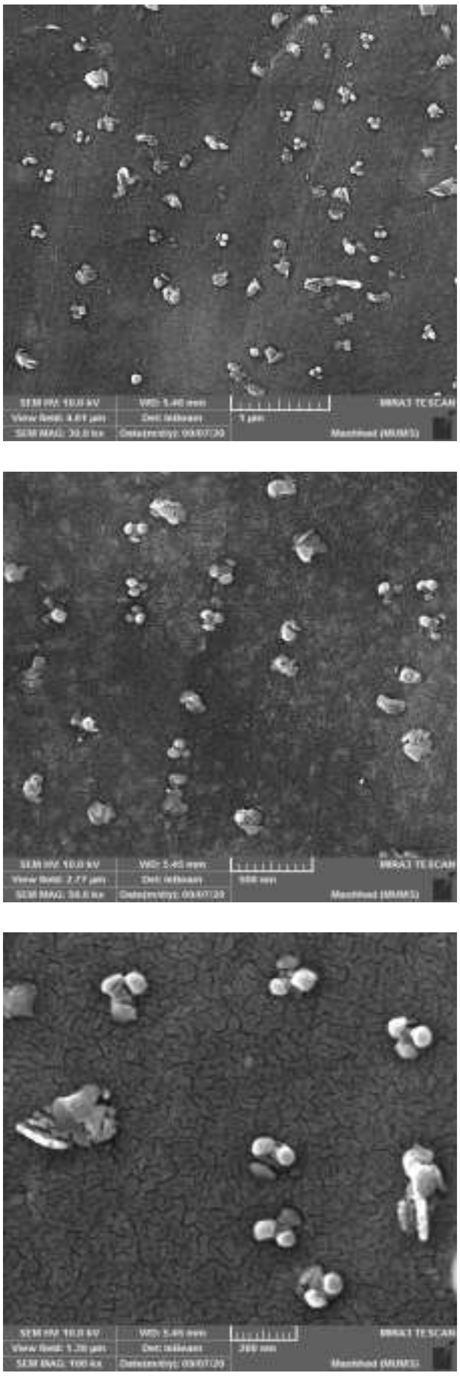

Fig. (10) SEM images of the nanostructured TiO_2 thin film prepared using Ar: O_2 gas mixture of 1:1 after deposition time of 2 hours

The prepared thin films were irradiate with 18W UV source in the spectral range 200-400nm and intensity of 10mW/cm^2 for two different intervals (15 and 30min). Contact angle measurements were performed in air using the sessile drop method. The contact angle of a water droplet on the surface was measured before irradiation with UV and after irradiation for 15 and 30min.

Figures (11) and (12) and table (2) show the results of contact angle of water droplet on the surfaces of undoped and Ni-doped TiO$_2$ samples. It was decreased after irradiation of the prepared samples for 15 and 30 minutes.

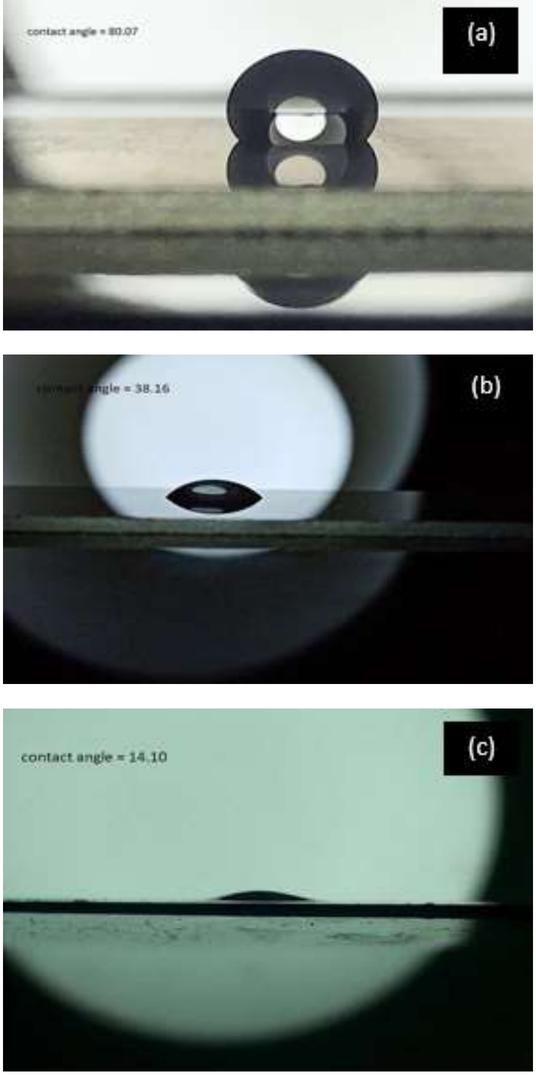

Fig. (11) Images of water droplet on the surface of undoped TiO$_2$ sample (a) before, (b) after 15 min. and (c) after 30 min. of UV irradiation

It was observed that the samples have high hydrophilicity that increases with increasing deposition time (i.e., film thickness). The good super-hydrophilic wetting and the antifogging effect were attributed to the highly accessible pores developed on the TiO$_2$ coated slide, on which the water droplets can be imbibed.

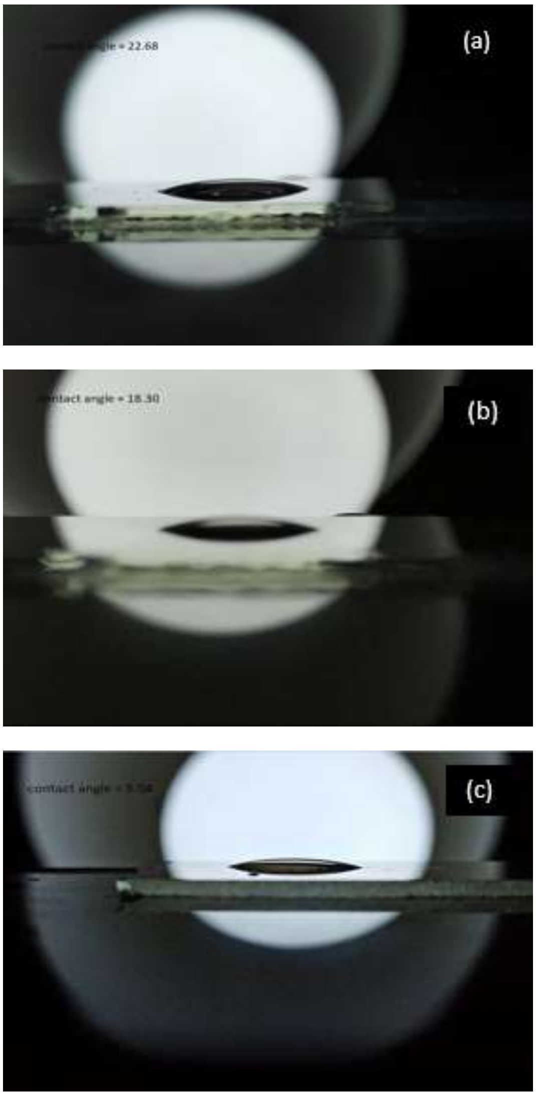

Fig. (12) Images of water droplet on the surface of Ni-doped TiO$_2$ sample (a) before, (b) after 15 min. and (c) after 30 min. of UV irradiation

Table (2) results of contact angle (θ_c) measurements of undoped and Ni-doped TiO$_2$ samples

Sample	θ_c before irradiation	θ_c after 15 min irradiation	θ_c after 30 min irradiation
Undoped TiO$_2$	80.07°	38.16°	14.1°
Ni-doped TiO$_2$	22.68°	18.30°	9.54°

4. Conclusions

Undoped and Ni-doped nanostructured TiO$_2$ thin films were prepared by dc reactive magnetron sputtering technique and deposited on glass substrates. The structures of the prepared thin films were mixed-phase and polycrystalline. These nanostructures were highly pure and homogeneous. The contact angle of a water droplet on the surfaces of undoped and Ni-doped TiO_2 thin films was decreased after 15 minutes of UV irradiation for all samples. The Ni-doped TiO_2 samples have high hydrophilicity that increases with increasing film thickness.

Reference

[1] C. Cantau et al., "N-doped TiO $_2$ by low temperature synthesis: Stability, photo-reactivity and singlet oxygen formation in the visible range," *J. Photochem. Photobiol. A Chem.*, 216(2-3) (2010) 201-208.

[2] J. Zhang et al., "New understanding of the difference of photocatalytic activity among anatase, rutile and brookite TiO_2," *Phys. Chem. Chem. Phys.*, 16(38) (2014) 20382-20386.

[3] C.C. Chen et al., "UV light induced photodegradation of malachite green on TiO_2 nanoparticles," *J. Hazard. Mater.*, 141(3) (2007) 520-528.

[4] N. Yuangpho et al., "The influence of experimental conditions on photocatalytic degradation of methylene blue using titanium dioxide particle," *J. Aust. Ceram. Soc.*, 54(3) (2018) 557-564.

[5] K.R. Zhu et al., "Size effect on phase transition sequence of TiO_2 nanocrystal," *Mater. Sci. Eng. A*, 403(1-2) (2005) 87-93.

[6] Y. Hu, H.L. Tsai and C.L. Huang, "Effect of brookite phase on the anatase-rutile transition in titania nanoparticles," *J. Eur. Ceram. Soc.*, 23(5) (2003) 691-696.

[7] S. Ardizzone et al., "Tailored anatase/brookite nanocrystalline TiO_2. the optimal particle features for liquidand gas-phase photocatalytic reactions," *J. Phys. Chem. C*, 111(35) (2007) 13222-13231.

[8] S.J. Shen, T.S. Yang, and M.S. Wong, "Co-sputtered boron-doped titanium dioxide films as photocatalysts," *Surf. Coatings Technol.*, 303 (2016) 184-190.

[9] W. Sangchay, L. Sikong and K. Kooptarnond, "The Photocatalytic and Antibacterial Activity of Cu-Doped TiO_2 Thin Films," 10(1) (2013) 19-27.

[10] W. Sangchay, "Contact angle of TiO_2/SnO_2 thin films coated on glass substrate," *Walailak J. Sci. Technol.*, 11(5) (2014) 429-436.

[11] M. Farbod and S. Rezaian, "An investigation of super-hydrophilic properties of TiO_2/SnO_2 nano composite thin films," *Thin Solid Films*, 520(6) (2012) 1954-1958.

[12] A. Nakajima et al., "Photoinduced amphiphilic surface on polycrystalline anatase TiO_2 thin films," *Langmuir*, 16(17) (2000) 7048-7050.

[13] T. Kamada et al., "Structure and properties of silicon titanium oxide films prepared by plasma-enhanced chemical vapor deposition method," *Jpn. J. Appl. Phys.*, 30(12) (1991) 3594-3596.

[14] A. Hu et al., "Hydrothermal growth of free standing TiO_2 nanowire membranes for photocatalytic degradation of pharmaceuticals," *J. Hazard. Mater.*, 189(1-2) (2011) 278-285.

[15] K.M. Reddy, S.V. Manorama and A.R. Reddy, "Bandgap studies on anatase titanium dioxide nanoparticles," *Mater. Chem. Phys.*, 78(1) (203) 239-245.

[16] M. Kanna and S. Wongnawa, "Mixed amorphous and nanocrystalline TiO_2 powders prepared by sol-gel method: Characterization and photocatalytic study," *Mater. Chem. Phys.*, 110(1) (2008) 166-175.

[17] H.K. Jang et al., "Titanium oxide films on Si(100) deposited by e-beam evaporation," *J. Vac. Sci. Technol. A Vacuum, Surf. Film.*, 18(6) (2000) 2932-2936.

[18] N. Inoue, H. Yuasa and M. Okoshi, "TiO_2 thin films prepared by PLD for photocatalytic applications," *Appl. Surf. Sci.*, 197-198 (2002) 393-397.

[19] M.K. Khalaf et al., "Crystalline structure and surface morphology of tin oxide films grown by DC reactive sputtering," *Photo. Sen.*, 4(4) (2014) 349-353.

[20] A. Hu et al., "Adsorption and photocatalytic degradation kinetics of pharmaceuticals by TiO_2 nanowires during water treatment," *Waste and Biomass Valorization*, 3(4) (2012) 443-449.

[21] S. Phromma et al., "Effect of calcination temperature on photocatalytic activity of synthesized TiO_2 nanoparticles via wet ball milling sol-gel method," *Appl. Sci.*, 10(3) (2020) doi: 10.3390/app10030993.

[22] K. Thamaphat, P. Limsuwan and B. Ngotawornchai, "Phase characterization of TiO_2 powder by XRD and TEM," *Kasetsart J.(Nat. Sci.)*, 42(5) (2008) 357-361.

[23] S. Liu et al., "Controllable sulfuration engineered NiO nanosheets with enhanced capacitance for high rate supercapacitors," *J. Mater. Chem. A*, 5(9) (2017) 4543-4549.

[24] F.J. Al-Maliki and N.H. Al-Lamey, "Synthesis of Tb-doped titanium dioxide nanostructures by sol–gel method for environmental photocatalysis applications," *J. Sol-Gel Sci. Technol.*, 81(1) (2017) 276-283.

[25] T. Lopez et al., "FTIR and UV-Vis (diffuse reflectance) spectroscopic characterization of TiO_2 sol-gel," *Mater. Chem. Phys.*, 32(2) (1992) 141-152.

[26] R.A. Aziz and I. Sopyan, "Synthesis of TiO_2-SiO_2 powder and thin film photocatalysts by sol-gel method," *Indian J. Chem. - Sect. A Inorganic, Phys. Theor. Anal. Chem.*, 48(7) (2009) 951-957.

[27] M.M. Kumar, S. Badrinarayanan and M. Sastry, "Nanocrystalline TiO_2 studied by optical, FTIR and X-ray photoelectron spectroscopy: Correlation to presence of surface states," *Thin Solid Films*, 358(1) (2000) 122-130.

IRAQI JOURNAL OF APPLIED PHYSICS
Vol. 17, No. 1, January-March 2021, pp. 9-16

Some Physical Properties of Metal-Hydroxyquinoline Complexes in Different Solvents

Atheer A.R. Mahmood [1]
Oday A. Hammadi [2]
Kais R. Ibraheem [3]

[1] *Department of Chemistry, College of Education, Al-Iraqia University, Baghdad, IRAQ*
[2] *Department of Physics, College of Education, Al-Iraqia University, Baghdad, IRAQ*
[3] *Department of Chemistry, College of Science, University of Anbar, Ramadi, IRAQ*

In this work, different organometallic complexes were prepared by linking metallic ions such as aluminum, barium, copper, manganese and zinc to 8-hydroxyquinoline ligand. The physical properties of these complexes in different solvents, mainly DMF and DMSO, were studied. Most complexes showed lower absorbance as well as lower refractive index when compared to those of 8-hydroxyquinoline in DMF or DMSO. Some samples showed comparable values due to the formation of nanoparticles within the prepared structures. As well, the zinc-hydroxyquinoline (Znq2) complex showed that two absorption edges with comparable intensities are formed. These results may encourage to consider these complexes for some spectroscopic applications such as laser dyes and random gain media.

Keywords: Hydroxyquinoline; Spectroscopy; Organometallic complex; Physical properties
Received: 22 February 2021; **Revised:** 13 March 2021; **Accepted:** 20 March 2021

1. Introduction

The 8-hydroxyquinoline (8-HQ) may be a cyclic compound ensuing from quinolone (1-azanaphthalene) and consists of 2 ring systems [1]. It is one phenolate a part of catecholate and one alkali donor of bipyridyl and is mirrored as a conjugate of 2 coordinating positions. It is thought about as monoanionic species and bridges the gap between the dianionic catecholate and therefore the neutral bipyridine [2].

A fast survey of the structure of 8-HQ reveals that it's -OH cluster and pyridyl N atom gift in 8-hydroxyquinoline that have the flexibility to act as a weak base and a weak acid underneath basic and acidic conditions, severally that is in a position to come with the equilibrium between quinolinate N~O in deprotonated type and quinolinium NH^+~OH within the protonated form [3].

Zinc complexes are particularly vital as a result of the simplicity in synthesis procedures and wide spectral response. In depth analysis work goes on in varied laboratories to synthesize new Zn complexes containing new ligands to supply variety of novel light zinc complexes [4-6].

Many complexes of 8-hydroxyquinoline such as AlQ_3, ZnQ_2, MgQ_2, ZnQ_2, and BeQ_2 have been extensively studied as emitters [7,8].

It is acknowledge that by substitution of a π-donor cluster akin to chemical element atom on the phenolate ring Associate in nursing an electron-withdrawing one on the alkali pyridine ring leads to red and blue shifted emissions [9-11].

8-Hydroxyquinoline is an organic compound with the formula C_9H_7NO. It is a derivative of the heterocycle quinoline by placement of an OH group on carbon number 8. 8-hydroxyquinoline (8-HQ) is a conjugated system and a bi functional hydrogen bonding molecule, in parotic solvents simultaneously acts as an H donor at the O-H group and as an H acceptor at the N atom [12].

The aluminium complex of 8-HQ, known as Alq_3 [13,14] has been applied to solar cells and optoelectronics [15]. Ruthenium complexes of 8-hydroxyquinoline are promising for catalysis in photosynthetic systems for fuel production [16].

It is known that Cr(III) and Al(III) have very similar ionic radii, coordination numbers (typically six) as well as comparable thermodynamic stabilities. In addition, 8-hydroxyquinolinate complexes of Cr(III) and Al(III) also exhibit excellent electronic spectral properties [17-20]. However, to the best of our knowledge, Cr(III) 8-hydroxyquinolates are rarely explored, even though 8-hydroxyquinoline shown excellent coordination ability with various metal ions [21,22].

In this work, organometallic complexes were prepared by direct mixing of 8-hydroxyquinoline ligand with some aqueous precursors to extract metals linked to this ligand and form the required complexes. Some physical properties and spectroscopic characteristics of the prepared complexes were determined. Such study is required to assess the performance of such complexes as fluorescent media in visible region of electromagnetic spectrum.

2. Experimental Part

Table (1) shows the chemicals and precursors used in this work to prepare the organometallic complexes. Table (2) shows the properties of the Dimethyl Formamide (DMF) and Dimethyl sulfoxide (DMSO) solvents used in this work to prepare the final samples for spectroscopic measurements.

Table (1) The chemicals and precursors used in this work

Chemical	Description
$AlCl_3.6H_2O$	Potassium alum
$KAl(SO_4)_2.12H_2O$	Aluminium chloride hexahydrate
$BaCl_2.2H_2O$	Barium chloride dihydrate
$CuCl_2.2H_2O$	Copper chloride dihydrate
$MnCl_2.4H_2O$	Manganese chloride tetrahydrate
$ZnCl_2$	Zinc chloride
$Zn(CH_3COO)_2{\cdot}2H_2O$	Zinc acetate dihydrate

Table (2) The properties of the DMF and DMSO solvents used in this work

	Polarity Index	Dipole Moment	Dielectric Constant
DMF	6.4	3.86	36.71
DMSO	7.2	4.1	46.68

A sample of 4.35g of 8-Hydroxyquinoline was dissolved in a mixture of 15 mL methanol and then it was stirred well till orange transparent solution was obtained. Separately, 3.75 g of $AlCl_3.6H_2O$ was dissolved in methanol, and stirred well till crystal transparent solution was obtained. These two solvents were mixed and the resultant suspension was stirred for 20 minutes. The other complex solutions such as Baq_2, Cuq_2, Mnq_2 and Znq_2, were prepared using the same method as used for Alq_3. As well, the mole ratios of 8-quinolinol to $Zn(CH_3COO)_2{\cdot}2H_2O$ was chosen as 2:1. Finally, the products were dried in oven at 60°C.

The absorbance of the prepared complexes was determined using UV-visible spectrophotometer in the spectral range of 200-900 nm. From these measurements, the refractive index of each complex was determined using suitable software.

Some samples were tested with the field-effect scanning electron microscopy (FE-SEM) in order to confirm the formation of nanoparticles within these samples. The effect of nanoparticle formation on the physical properties of prepared complexes was introduced.

3. Results and Discussion

Figure (1) shows the absorption spectra of the 8-hydroxyquinoline (8-Hq) ligand dissolved in two different solvents (DMF and DMSO). It is clear that this ligand shows high absorbance in the ultraviolet (UV) wavelengths shorter than 340 nm before a fast decrease to be approximately transparent at 380 nm and longer wavelengths (visible region). However, the 8-Hq dissolved in DMSO shows higher absorbance (>100%) than that in DMF. This may be attributed to the properties of these solvents mainly polarity index, dipole moment, and dielectric constant.

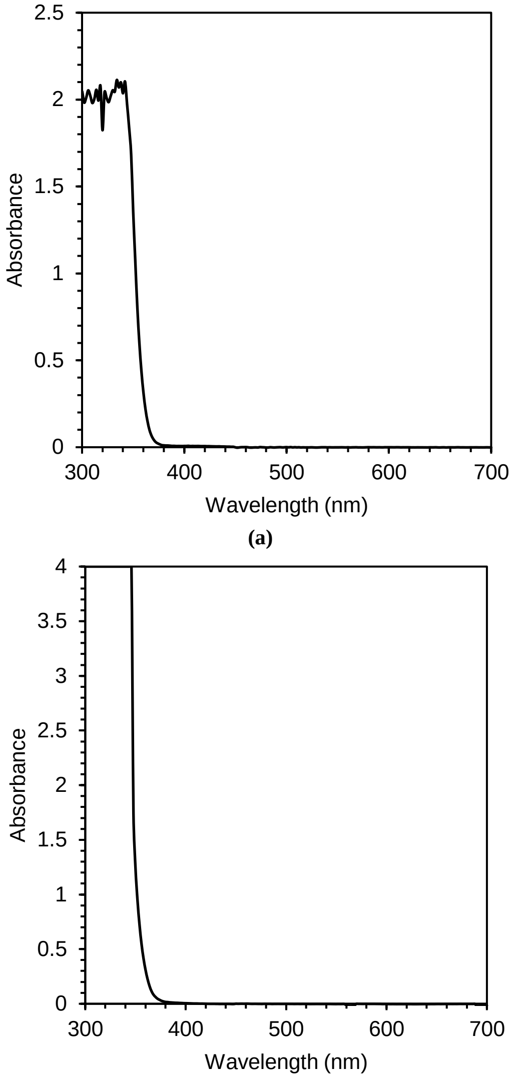

(a)

(b)

Fig. (1) Absorbance of 8-hydroxyquinoline ligand in different solvents (a) DMF and (b) DMSO

In similar way, the values of refractive index of the 8-Hq ligand in two different solvents (DMF and DMSO) were determined and compared as shown in Fig. (2). At wavelengths shorter than 345 nm, the 8-Hq in DMF shows higher value of refractive index than that in DMSO. However, the maximum value of refractive index about 1.5 was determined at 352 nm for both cases. Also, both samples show identical behavior in the visible region (380-700 nm). Accordingly, the effect of solvent was clearly observed in the UV region.

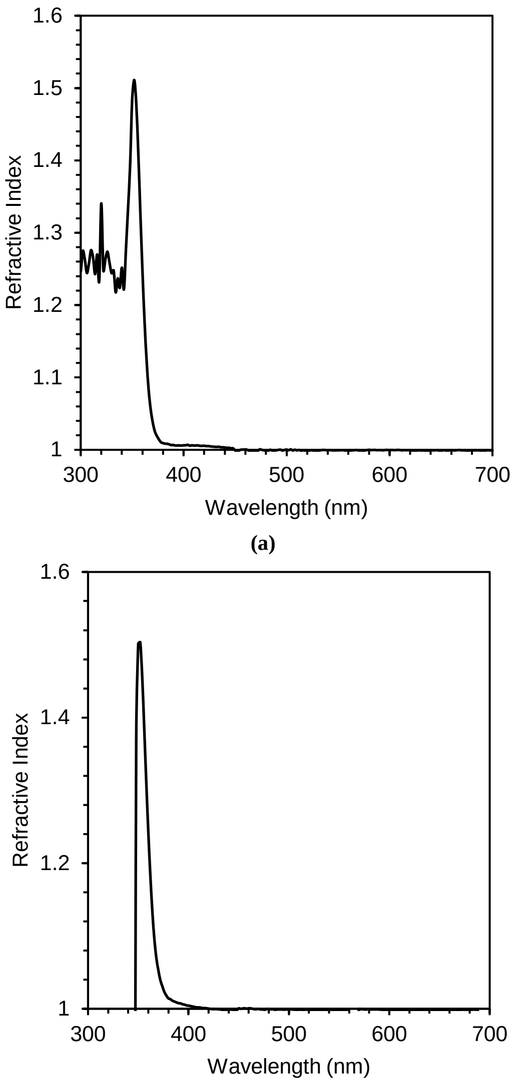

(a)

(b)

Fig. (2) Variation of refractive index of 8-hydroxyquinoline ligand in different solvents (a) DMF and (b) DMSO

The absorption spectra of organometallic complexes (Alq$_3$, Baq$_2$, Cuq$_2$, Mnq$_2$ and Znq$_2$) in DMF are presented in Fig. (3). Table (3) shows the absorption edges of the 8-Hq ligand and prepared complexes in DMF. Similarly, the absorption spectra of organometallic complexes (Alq$_3$, Baq$_2$, Cuq$_2$, Mnq$_2$ and Znq$_2$) in DMSO are presented in Fig. (4). Table (4) shows the absorption edges of the 8-Hq ligand and prepared complexes in DMSO. The summary of these results are shown in Fig. (5).

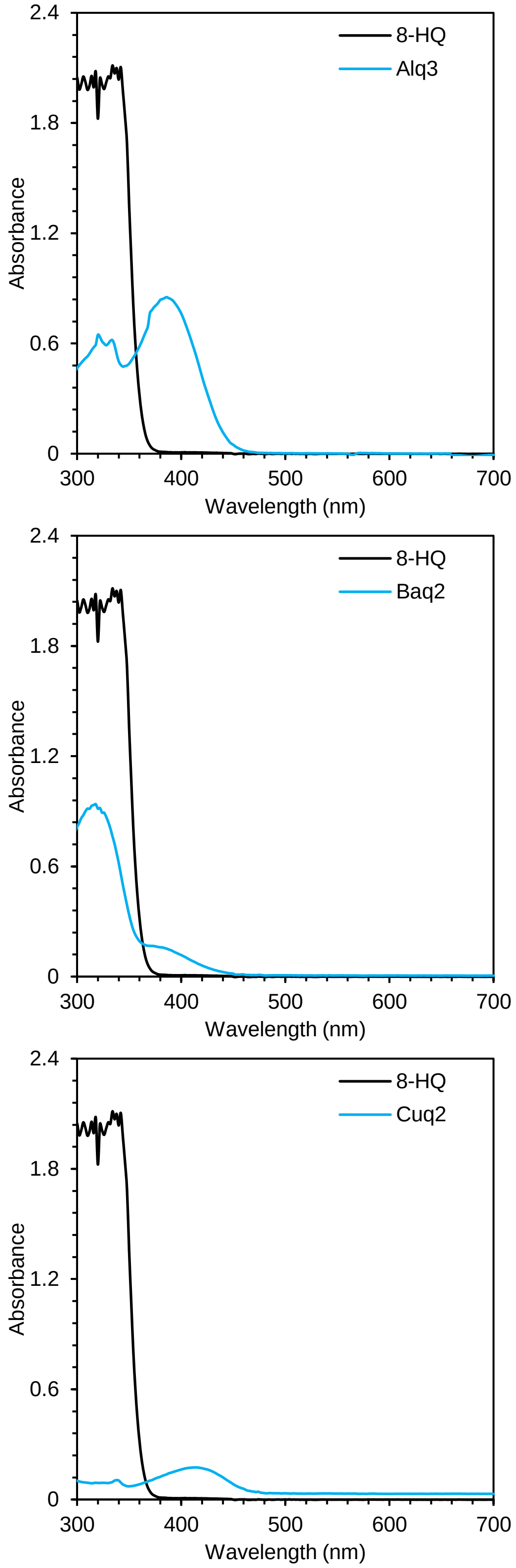

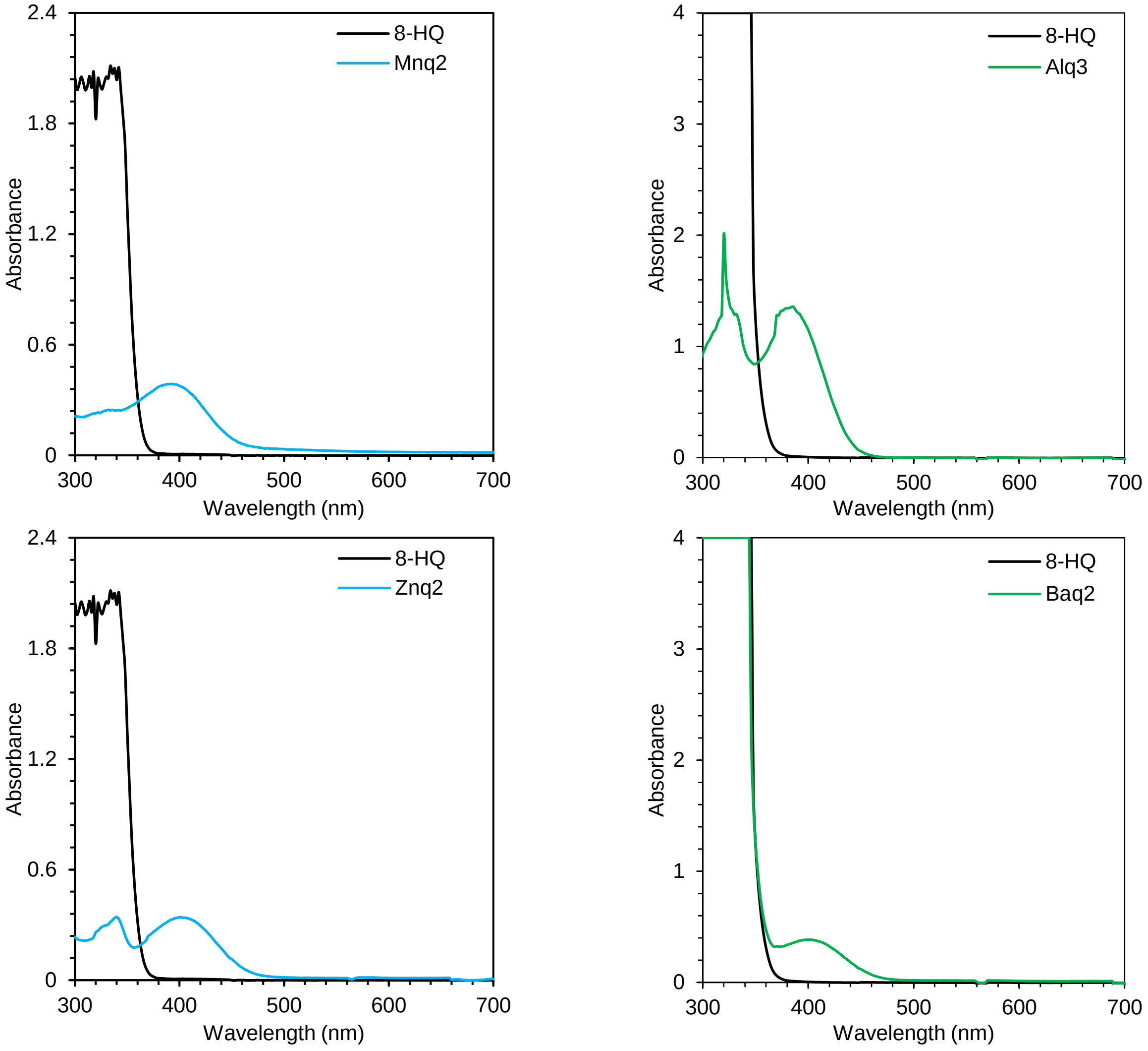

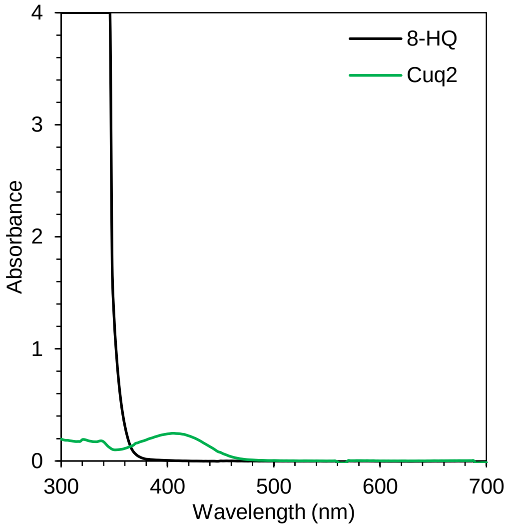

Fig. (3) Absorbance of the M-8-hydroxyquinoline complexes prepared in this work in DMF

It is clear that the type of solvent has no effect on the absorption edge of the Alq_3 complex, has slight effect on the absorption edge of the Cuq_2 and Mnq_2 complexes, and reasonable effect on the absorption edge of the Baq_2 complex. The Znq_2 shows two comparable absorption edges at 340 and 400 nm in DMF and at 338 and 400 nm in DMSO. Also, in general, the organometallic complexes show shift in absorption edge towards longer wavelengths. However, the Baq_2 in DMF shows irregular behavior as the absorption edge was simply decreased by ~100% (at 318nm) when compared to the absorption edge of the 8-Hq in DMF (at 334nm).

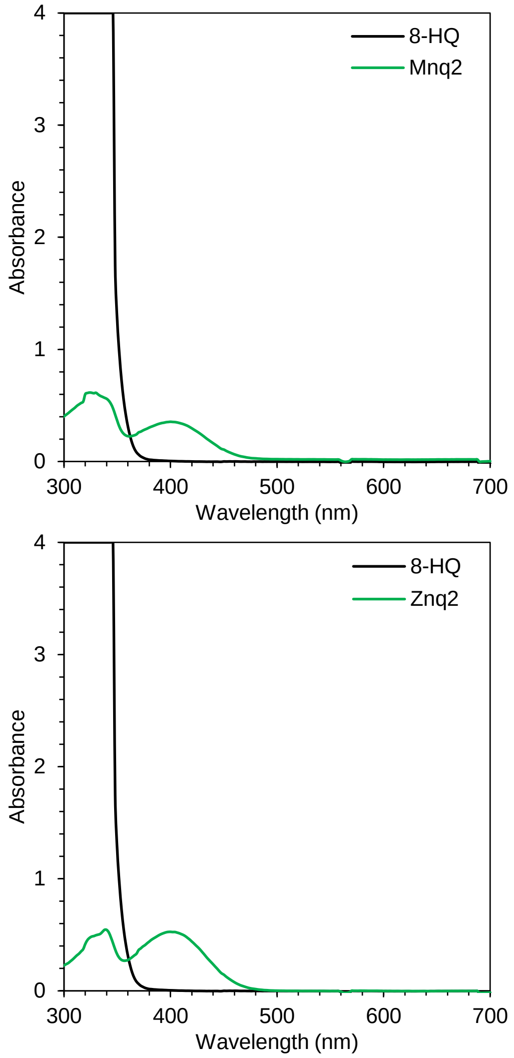

Fig. (4) Absorbance of the M-8-hydroxyquinoline complexes prepared in this work in DMSO

Table (3) Absorption peaks of the prepared complexes compared to that of 8-Hq in DMF

Complex	Absorption Peak	Absorption Edge (nm)
8-Hq in DMF	2.113	334
Alq$_3$	0.852	386
Baq$_2$	0.938	318
Cuq$_2$	0.174	414
Mnq$_2$	0.387	392
Znq$_2$	0.342	340
	0.341	400

Table (4) Absorption peaks of the prepared complexes compared to that of 8-Hq in DMSO

Complex	Absorption Peak	Absorption Edge (nm)
8-Hq in DMSO	4	346
Alq$_3$	1.356	386
Baq$_2$	0.385	402
Cuq$_2$	0.247	406
Mnq$_2$	0.354	400
Znq$_2$	0.544	338
	0.526	400

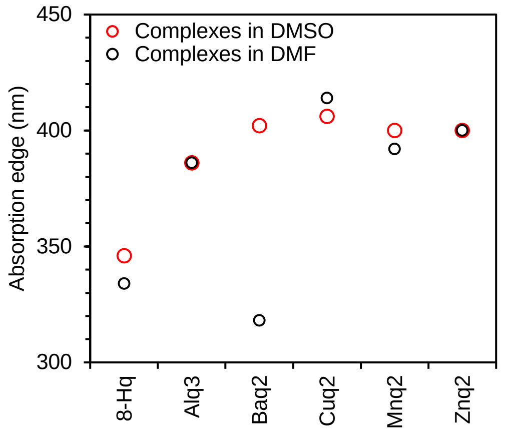

Fig. (5) Summary of absorption edges of the 8-Hq and prepared complexes in two different solvents (DMF and DMSO)

In similar manner, the refractive index of each complex prepared in this work was compared to that of 8-Hq in two different solvents (DMF and DMSO). These results are shown in figures (6) and (7) and the summary is shown in tables (5) and (6).

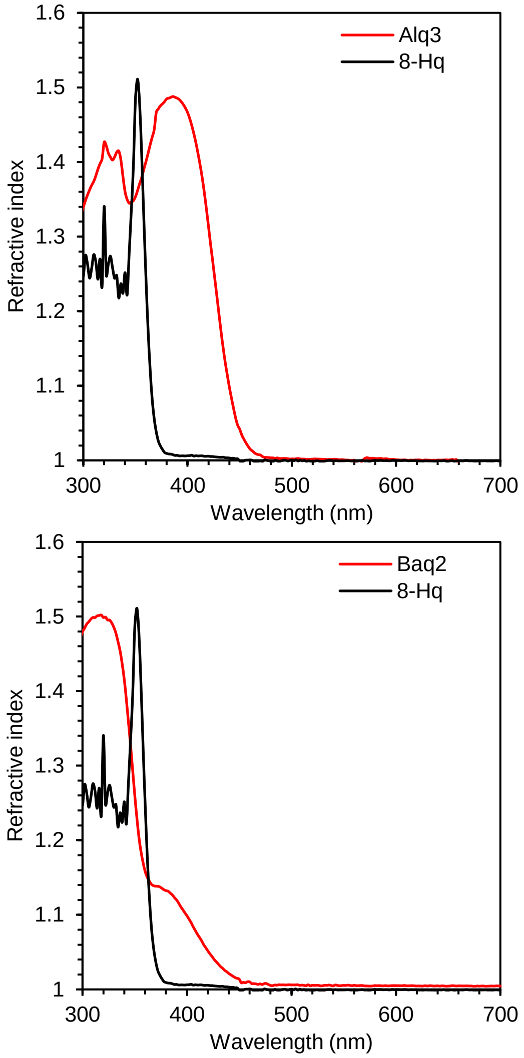

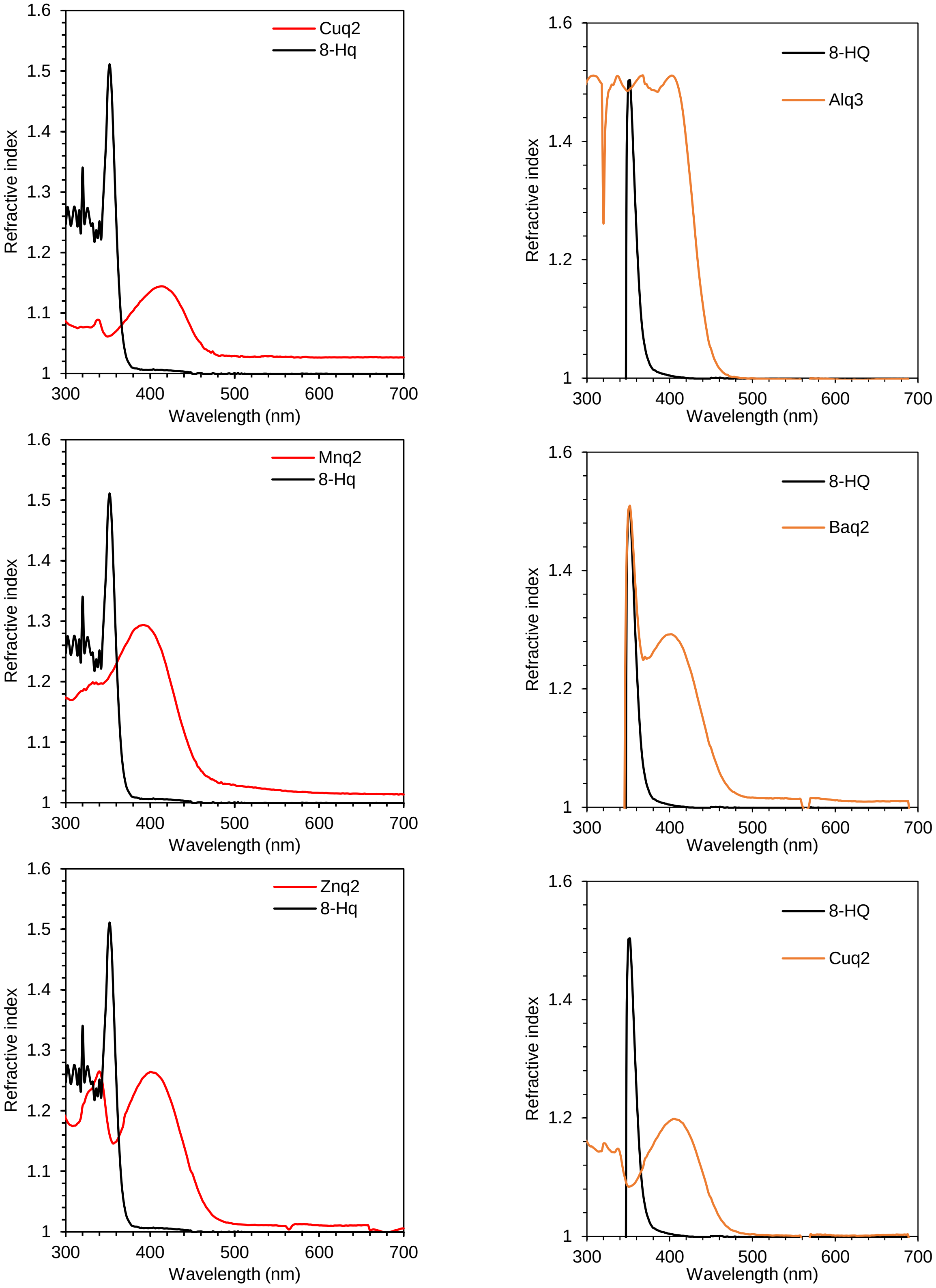

Fig. (6) Variation of refractive index of the M-8-hydroxyquinoline complexes prepared in this work in DMF

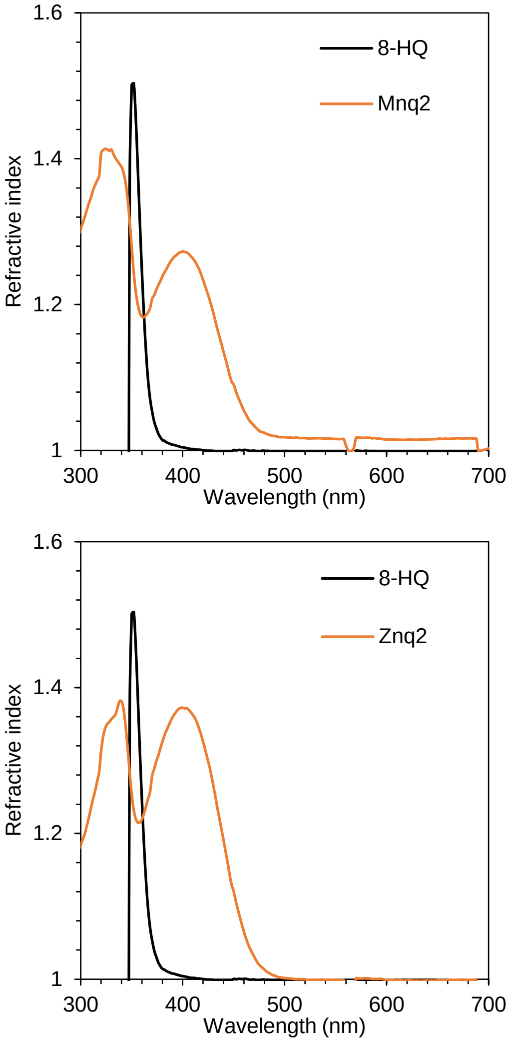

Fig. (7) Variation of refractive index of the M-8-hydroxyquinoline complexes prepared in this work in DMSO

In general, all prepared complexes have lower values of refractive index when compared to the 8-Hq in DMF or DMSO. This is attributed to the linkage of metallic ions to the ligand. However, the Baq_2 in DMF and Alq_3 in DMSO have refractive indices comparable to that of 8-Hq in either DMF or DMSO. This result agrees to that of absorption shown before.

In order to interprete the different behaviors of Alq_3 and Baq_2 complexes, the FE-SEM has confirmed the formation of nanoparticles in these samples with minimum particle size of 8.2 and 49.4 nm for Alq_3 and Baq_2, respectively, while other complexes, such as Znq_2, shows reasonably larger particles. These nanoparticles are highly expected to play a key role in the spectroscopic properties of the prepared complexes due to the quantum size effect.

Table (5) Refractive indices of the prepared complexes compared to that of 8-Hq in DMF

Complex	Maximum Refractive index	@ nm
8-Hq in DMF	1.488	382
Alq_3	1.487	386
Baq_2	1.502	318
Cuq_2	1.144	414
Mnq_2	1.293	392
Znq_2	1.265	340
	1.264	400

Table (6) Refractive indices of the prepared complexes compared to that of 8-Hq in DMSO

Complex	Maximum Refractive index	@ nm
8-Hq in DMSO	1.503	352
Alq_3	1.511	402
Baq_2	1.292	402
Cuq_2	1.198	406
Mnq_2	1.273	400
Znq_2	1.381	338
	1.371	404

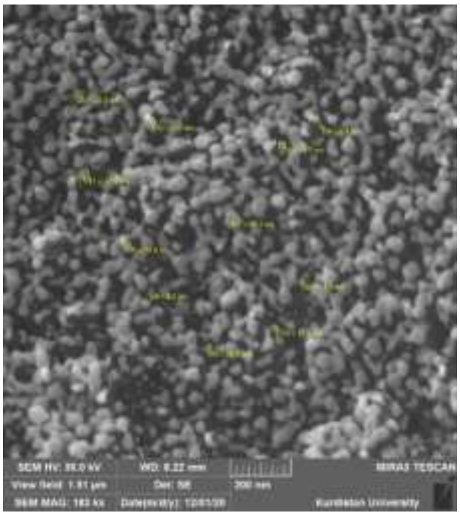

Alq_3

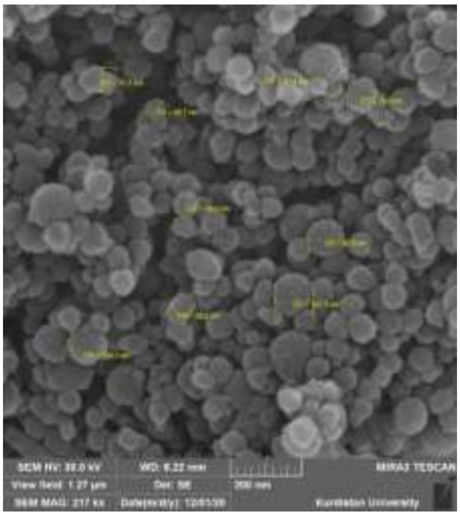

Baq2

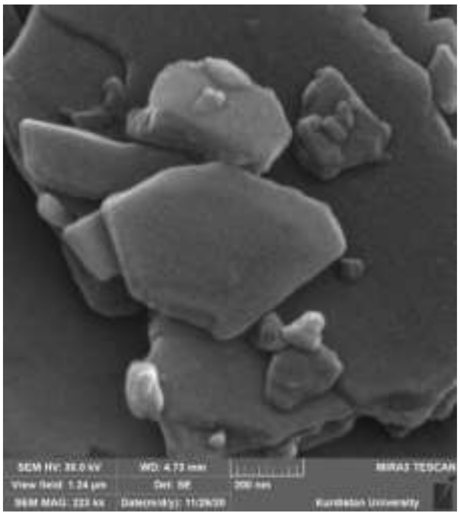

Znq2

Fig. (8) FE-SEM images of some M-8-hydroxyquinoline complexes prepared in this work

4. Conclusion

In concluding remarks, the properties of solvent, such as polarity index, dipole moment and dielectric constant, have affected the physical properties of organometallic complexes, especially absorption and refractive index in the spectral range 300-800 nm. Linkage of metal ions to the ligand structure has lead in general to decrease the absorbance as well as the refractive index of the prepared complex. The formation of nanoparticles within the complex structure was found to have reasonable effect on these properties due to the quantum size effect.

References

[1] A. Godard, Y. Robin and G. Queguiner, J. Organomet. Chem., 336 (1987) 1-12.

[2] D.J. Berg, S.J. Rettig and C. Orvig, J. Am. Chem. Soc., 113 (1991) 2528-2532.

[3] Y. Mei, P.A. Bentley and W. Wang, Tetrahedron Lett., 47 (2006) 2447-2449.

[4] S.F. Liu et al., J. Am. Chem. Soc., 122 (2000) 3671-3678.

[5] Q. Wu, J.A. Lavigne and S. Wang, Inorg. Chem., 39 (2000) 5248-5254.

[6] Y.K. Jang et al., J. Korean Phys. Soc., 49 (2006) 1057-1061.

[7] Y. Hamada et al., Jpn. J. Appl. Phys., 32 (1993) L514-L515.

[8] C.H. Cheng and S. Jianmin, Coord. Chem. Rev., 171 (1998) 161-174.

[9] R. Pohl et al., J. Org. Chem., 69 (2004) 1723-1725.

[10] R. Pohl and P. Anzenbacher Jr., Org. Lett., 5 (2003) 2769-2772.

[11] Y. Fazaeli et al., J. Colloid. Interface Sci., 346 (2010) 384-390.

[12] A. Bach et al., J. Chem. Phys., 112(3) (2000) 1192-1198.

[13] C.W. Tang and S.A. van Slyke, Appl. Phys. Lett., 51 (1987) 913-915.

[14] M. Colle, R.E. Dinnebier and W. Brutting, Chem. Commun., (2002) 2908-2909.

[15] L.G.C. Rego et al., J. Phys. Chem. C, 114(2) (2010) 1317-1325.

[16] L. Duan et al., Acc. Chem. Res., 48(7) (2015) 2084-2096.

[17] P.S. Wagenknecht and P.C. Ford, Coordin. Chem. Rev., 255 (2011) 591-616.

[18] L.S. Forster, Coordin. Chem. Rev., 248 (2004) 261-272.

[19] W.A.E. Omar and O.E.O. Hormi, Tetrahedron, 65 (2009) 4422-4428.

[20] V.P. Barberis and J.A. Mikroyannidis, Synth. Met., 156 (2006) 865-871.

[21] B. Li et al., Inorg. Chim. Acta, 366 (2011) 241-246.

[22] C. Lima et al., Phys. Chem. Chem. Phys., 18 (2016) 16555-16565.

IRAQI JOURNAL OF APPLIED PHYSICS
Vol. 17, No. 1, January-March 2021, pp. 17-20

Comparative Study of Structural and Optical Properties of Silicon Dioxide Nanoparticles Prepared by DC Reactive Sputtering and Sol-Gel Route

Nora H. Mutesher
Firas J. Kadhim

Department of Physics,
College of Science,
University of Baghdad,
Baghdad, IRAQ

In the present work, nanostructured silicon dioxide thin films were synthesized using two different deposition techniques: sol-gel and dc reactive plasma sputtering. Amorphous structural phase of silica films was observed for the samples synthesized by both methods. The scanning electron microscopy indicated that the average particle size of samples prepared by plasma sputtering was smaller than that of samples prepared sol-gel. The spectroscopic measurements confirmed the formation of siloxane bonds as well as the high content of hydroxyl groups in samples prepared by sol-gel while those prepared by plasma sputtering showed lower content of OH while siloxane was not found in the final sample at all. Energy band gap was determined and found to be 4.57 eV for sample prepared by sol-gel and 3.82 eV for samples prepared by plasma sputtering. These results highlight the advantages of plasma sputtering technique over sol-gel as thin film deposition methods.

***Keywords*: Silicon dioxide; nanostructures; Reactive magnetron sputtering; Sol-gel**
Received: 01 March 2021; **Revised:** 21 March; **Accepted:** 28 March 2021

1. Introduction

In recent years, nanoparticles have attracted much attention because to their distinct properties that make them suitable for different applications including catalysts, humidity sensors, pigments and pharmaceuticals [1,2]. Silicon dioxide or silica (SiO_2) nanostructures have represented excellent choice in scientific and industrial applications due of its ease of production and appropriateness for a wide range of uses such as anti-resistance, corrosion resistance, stiffness, dielectric and optical transparency [3-5]. The industrial silica (silica gels, acidic silica and precipitated silica) is pure and can be produced as powder with amorphous structure compared to natural silica that is crystalline like quartz [6].

There are several physical and chemical deposition methods used to prepare silica thin films such as reactive sputtering [7-10], spray pyrolysis [11], anodization [12] and sol–gel [13-16]. Among these methods, sol-gel is a chemical wet method includes changing the composition and viscosity of the sol, and the thickness of the prepared film can be reasonably controlled. Final product may be shaped in several structural forms by controlling gelation conditions and can be supported with different materials. Sol-gel is usually used to prepare amorphous phase with drying at 250 °C. There are several factors that influence the final product of sol-gel such as pH, temperature, time, molar ratios of reactants, and properties of solvent [17].

On the other hands, the dc reactive plasma sputtering technique is highly interesting for industrial purposes for many reasons, mainly; metal alloys can be synthesized as thin films, formation and thickness of the prepared films can be controlled [18], and large-scale production is possible [19]. There are many factors affecting sputtering technique such as gas pressure, gas mixing ratio, flow rate, substrate biasing, inter-electrode distance, discharge power, etc. [14-18].

The goal of the present work is to compare the optical and structural characteristics of silica nanoparticles synthesized by two different deposition techniques; sol-gel and dc reactive plasma sputtering. Such comparison is very important to make these nanoparticles applicable in several applications.

2. Experimental Part

The Synthesis of silica thin films by sol-gel method includes mixing ethanol and tetraethylorthosilicate (TEOS, Sigma-Aldrich, 98%) with a molar ratio of 1:4 to prepare the first mixture. The catalyst mixture was containing deionized water calibrated to certain pH value by addition of 0.15 M of hydrochloric acid (HCl, >95%) mixed with ethanol (EthOH, Fluka Grantie, 99.9%) at molar ratio of 2:4. Then, the catalyst mixture was added dropwise to the first mixture to form the final sol. Finally, 0.5 ml of N,N-dimethaylformamide (99%) was added to the final sol as drying-control chemical additive, then casting in a covered glass tube at 60 °C aging for 2 hours. After that, the silica films were prepared by placing drops of the sol on substrate with spinning speed of 3500 rpm by spin coating system and dried the film at 60 °C for 2 hours.

Synthesis of silica thin films using dc closed-field unbalanced magnetron (CFUBM) reactive plasma sputtering technique was carried out as follows. A p-type silicon wafer of 6cm diameter was linked to the cathode inside deposition chamber as a target and the glass substrate was placed on the anode. The deposition chamber was initially evacuated down to ~0.01 mbar using double-stage rotary pump. The operation parameters of the sputtering configuration include total gas pressure in the range 0.06-0.1 mbar, inter-electrode distance of 4 cm, Ar:O_2 gas mixing ratio of 1:1, gas flow rate of 1 sccm. The applied voltage could be varied during operation in order to control the discharge current at 40 mA. In the chamber, after reaching the operating pressure of 0.01 mbar, the gas mixture of discharge (argon) and reactive (oxygen) gases were pumped into chamber and the plasma was generated at breakdown voltage of about 290V. Deposition time was 3 hours.

The structural and optical characteristics of the silica thin films prepared by both techniques were studied by the x-ray diffraction (XRD) using Shimadzu diffractometer with Cu Kα radiation (λ=1.54060Å) at 40.0 kV and 30 mA, scanning electron microscopy (SEM), Fourier-transform infrared (FTIR) spectrometry using Shimadzu 8400S spectrometer, and UV-Visible spectrometry using Visual Spectrometry 2.1Sr (Korea).

3. Result and Discussion

The XRD analysis was performed on the prepared samples and typical diffraction patterns are shown in Fig. (1). It is clearly observed that the samples prepared by both methods have amorphous structures because the XRD diagrams did not show patterns emerging from the crystalline phases. Silica are mostly exhibit amorphous structure when prepared by common deposition techniques. However, crystalline silica can be synthesized by crystal growth processes.

The vibrational bands of silica were found in the FTIR spectra of thin film samples as seen in Fig. (2). These spectra show common bands, a broad band centered at 3400 cm^{-1} is ascribed to stretching vibrations of the free silanol group Si-OH on the surface of silica network and the hydroxyl groups of adsorbed water [20]. The bands around ~460 (466) cm^{-1} match to the bending mode of Si-O-Si bond and the band around ~802 cm^{-1} match to the symmetric vibration of Si-O bond. The situation and the form of Si-O vibrational band around 1072 (1063) cm^{-1} refer to asymmetric vibration appears a stoichiometric silicon dioxide structure [21-23].

Figure (3) illustrates the UV-Visible absorption spectra of silica thin films synthesized by sol-gel and plasma sputtering. The absorption edge is 339 nm for the samples prepared by sol-gel and 352 nm for the samples prepared by sputtering. The absorption of silica thin films is highly dependent on the transparency (or thickness) of the film. It can be seen that the intensity of the absorption spectrum of pure silica continuously decreases with wavelength without any peaks [25,26].

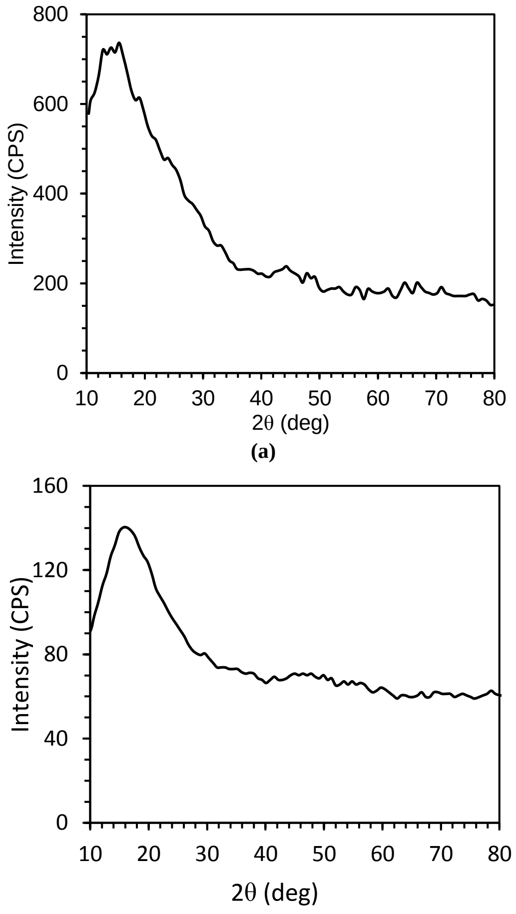

(a)

(b)

Fig. (1) XRD patterns of silica thin film samples prepared by (a) dc reactive sputtering, and (b) sol-gel

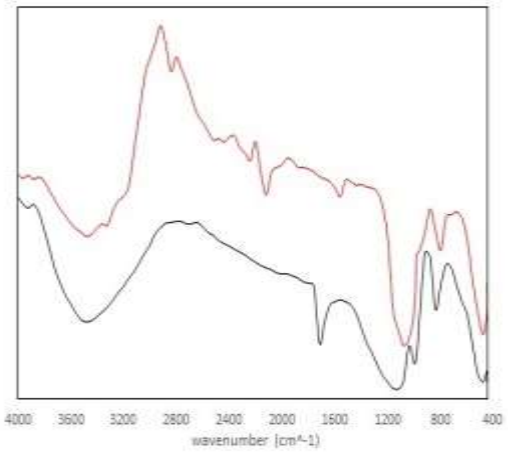

Fig. (2) FTIR spectra of silica thin film samples prepared by sol-gel (black line) and by dc reactive sputtering (red line)

We can conclude from the figure above that the plasma sputtering technique is better because of the high homogeneity, as well as lower OH groups, i.e., less porosity.

Using Tauc's equation, the band gap energy of prepared thin film samples can be determined as:

$$(\alpha h\nu)^{1/n} = A\,(h\nu - E_g)$$

where h is the Planck's constant, ν is the photon frequency, E_g is the band gap energy, and A is a constant

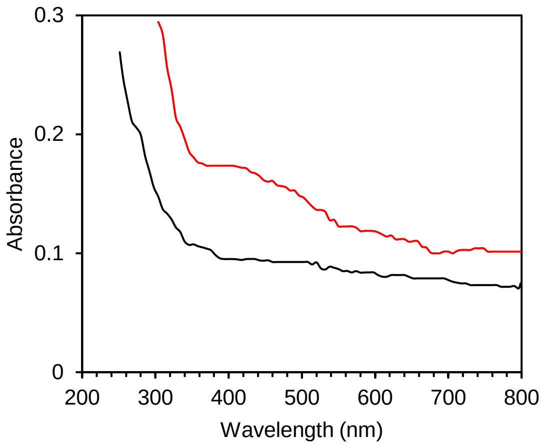

Fig. (3) Absorption spectra of silica thin film samples prepared by sol-gel method (black line) and by dc reactive sputtering (red line)

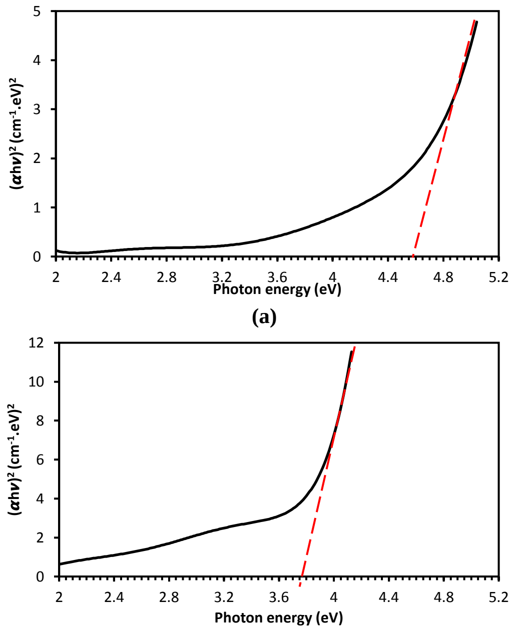

(a)

(b)

Fig. (4) Determination of energy band gap for silica thin film samples prepared by (a) sol-gel, and (b) dc reactive sputtering

The value of n depends on the nature of the electron transition and is equal to 0.5 or 2 for the direct and indirect transition band gaps, respectively [27]. The energy band gap was determined to be 3.82 eV for the sample prepared by plasma sputtering and 4.57 eV for the sample prepared by sol-gel as shown in Fig. (4).

Figure (5) shows the SEM micrographs of the silica samples prepared in this work by both methods. The SEM micrographs in Fig. (5a) shows silica nanoparticles prepared by sol-gel method. It can be observed that the average particle size is 26.8 nm. Figure (5b) shows silica nanoparticles prepared by plasma sputtering technique. The average particle size is 18 nm. This large difference in average particle size can be considered as an advantage of sputtering technique in nanostructure fabrication. It also can be seen that the aggregation over the prepared nanoparticles is relatively low [28].

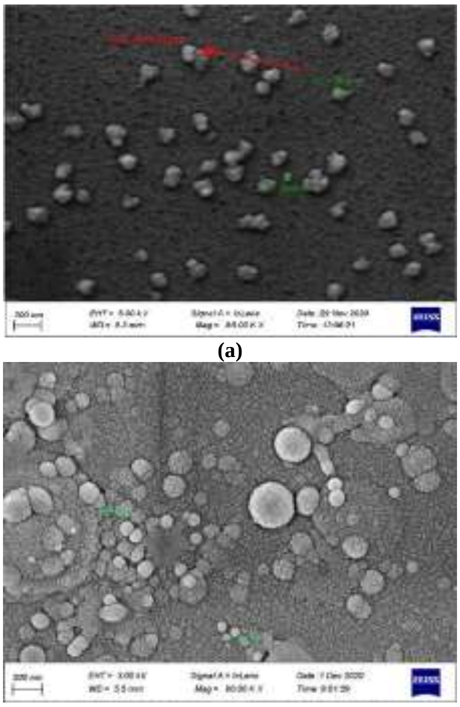

(a)

(b)

Fig. (5) SEM micrographs of silica nanoparticles prepared by (a) sol-gel, and (b) dc reactive sputtering

4. Conclusion

In concluding remarks, the structural and optical properties of the nanostructured silicon dioxide thin films synthesized by sol-gel method and sputtering technique have been compared. Silicon dioxide nanostructures prepared in this work was same amorphous and have one peak in all two methods. Spectroscopic studies showed that the SiO_2 compound was formed in both methods but with lower OH groups, little aggregation and higher homogeneity of nanoparticles prepared by sputtering technique. The band gap energy of the film samples prepared by plasma sputtering (3.82 eV) was lower than that prepared by sol-gel (4.57 eV). Accordingly, we can conclude that plasma sputtering technique is better to synthesize silica due to high uniformity of film thickness, good control of deposition rate, good adhesion of film to substrate and good optical properties.

References

[1] K.S Rao et al., "A novel method for synthesis of silica nanoparticles", J. Colloid Interface Sci., 289 (2005) 125-131.

[2] I.A Rahman et al., “Synthesis of silica nanoparticles by modified sol-gel process: The effect of mixing modes of the reactants and drying techniques”, J. Ceram. Int., 50(3) (2006) 328-336.

[3] J. Chrusciel and L. Slusarski, “Synthesis of nanosilica by the sol-gel method and its activity toward polymers”, J. Mater. Sci., 21(4) (2003) 461-469.

[4] K. Kim and D.H.T Kim, “Formation of Silica Nanoparticles by Hydrolysis of TEOS Using a Mixed Semi-Batch/Batch Method”, J. Sol-Gel Sci. Technol., 25 (2002) 183-189.

[5] S. Tabatabaei et al., “Experimental study of the synthesis and characterisation of silica nanoparticles via the sol-gel method”, J. Phys.: Conf. Series, 26 (2005) 371-374.

[6] E.F. Vansant, P.V.D. Voort and K.C. Vrancken, **“Characterization and Chemical Modification of the Silica Surface”**, Elsevier Science (NY, 1995) p. 553.

[7] M. Radecka et al., “Influence of Cr on photoelectrochemical properties of TiO_2 thin films”, Physica B, 348 (2004) 160-168.

[8] A. Gorzkowska et al., “Visible photocurrent response of TiO_2 anode”, Surf. Sci., 600 (2006) 3694-3970.

[9] A. Brudnik et al., “Thin film TiO_2 photoanodes for water photolysis prepared by dc magnetron sputtering”, J. Power Sources, 173 (2007) 774-780.

[10] M. Radecka et al., “Importance of the band gap energy and flat band potential for application of modified TiO_2 photoanodes in water photolysis”, J. Power Sources, 181 (2008) 46-55.

[11] P.S. Shinde et al., “Properties of spray deposited titanium dioxide thin films and their application in photoelectrocatalysis”, Sol. Energy Mater. Sol. Cells, 92 (2008) 283-290.

[12] W.K. Zhang et al., “Light energy storage and photoelectrochemical behavior of the titanate nanotube array/$Ni(OH)_2$ electrode”, Electrochim. Acta, 54 (2009) 4760-4763.

[13] J. Chen et al., “Improving the photoelectrochemical performance of polythiophene sensitized TiO_2 electrode by modification with gold nanoparticles”, Chem. Phys. Lett., 460 (2008) 168-172.

[14] P.R. Mishra et al., “Investigation and optimization of nanostructured TiO_2 photoelectrode in regard to hydrogen production through photoelectrochemical process”, Int. J. Hydrogen Energy, 28 (2003) 1089-1094.

[15] M. Bockmeyer and P. Lobmann, “Densification and Microstructural Evolution of TiO_2 Films Prepared by Sol−Gel Processing”, Chem. Mater, 18 (2006) 4478-4485.

[16] P.R. Mishra, P.K. Shukla and O.N. Srivastava, “Study of modular PEC solar cells for photoelectrochemical splitting of water employing nanostructured TiO_2 photoelectrodes”, Int. J. Hydrogen Energy, 32 (2007) 1680-1685.

[17] T. Sugimoto, X. Zhou and A. Muramatsu, “Synthesis of uniform anatase TiO_2 nanoparticles by gel–sol method: 3. Formation process and size control”, J. Colloid Interface Sci., 259 (2003) 43-52.

[18] M. Matsuoka et al., “Photocatalysis for new energy production: recent advances in photocatalytic water splitting reactions for hydrogen production”, Catal. Today, 122 (2007) 51-61.

[19] L. Dreesen et al., “DC Magnetron Sputtering Deposition of Titanium Oxide Nanoparticles: Influence of Temperature, Pressure and Deposition Time on the Deposited Layer Morphology, the Wetting and Optical Surface Properties”, Thin Solid Films, 6 (2009) 849-854.

[20] S. Sotiropoulou and N.A. Chaniotakis, “Tuning the sol–gel microenvironment for acetylcholinesterase encapsulation”, Biomaterials, 26 (2005) 6771-6779.

[21] P. Paik, A. Gedanken and Y. Mastai, “Enantioselective Separation Using Chiral Mesoporous Spherical Silica Prepared by Templating of Chiral Block Copolymers”, ACS Appl. Mater. Interfaces, 8 (2009) 34-42.

[22] P. Paik, A. Gedanken and Y. Mastai, “Chiral separation abilities: Aspartic acid block copolymer-imprinted mesoporous silica”, J. Phys. Chem. B, 111 (2007) 11105-11110.

[23] P. Paik et al., “Synthesis of amino acid block-copolymer imprinted chiral mesoporous silica and its acoustically-induced optical Kerr effects”, J. Solid State Chem., 192 (2012) 127-131.

[24] B. Window and N. Sawides, “Unbalanced dc magnetrons as sources of high ion fluxes", J. Vac. Sci. Technol. A, 4(2) (1986) 453-457.

[25] Y. Ren et al., “Facile synthesis of Au@SiO_2core-shell nanoparticles with multiple Au nanodots by a reverse microemulsion (water-in-oil) method”, Coll. Surf. A: Physicochem. Eng. Aspects, 486 (2015) 14-20.

[26] S. Veeranarayanan et al., “FITC labeled silica nanoparticles as efficient cell tags: uptake and photostability study in endothelial cells”, J. Fluoresc., 22 (2011) 537-548.

[27] J.I. Pankove, **“Optical Processes in Semiconductors”**, Prentice-Hall, Englewood Cliffs (NJ, 1971).

[28] H.G. Fahad and O.A. Hammadi, “Characterization of Highly-Pure Silicon Dioxide Nanoparticles as Scattering Centers for Random Gain Media”, Iraqi J. Appl. Phys., 16(2) (2020) 37-42.

[29] M.A. Hameed and Z.M. Jabbar, “Preparation and Characterization of Silicon Dioxide Nanostructures by DC Reactive Closed-Field Unbalanced Magnetron Sputtering”, Iraqi J. Appl. Phys., 12(4) (2016) 13-18.

IRAQI JOURNAL OF APPLIED PHYSICS
Vol. 17, No. 1, January-March 2021, pp. 21-24

Maher M. Jassim
Alaa O. Hussain

Department of Physics,
College of Science,
University of Babylon,
Hilla, IRAQ

Experimental Considerations for Diffusion of Metals into Silicon for Integrated Circuit Interconnects

In this study, the concentration profiles for unsteady-state and drive-in diffusion conditions into semiconductors taken at different times were considered and compared. As well, the diffusion of copper, gold, silver, and aluminum in silicon was determined using the analytical expressions derived from Fick's law of diffusion. These situations were compared to the experimental situation of boron diffusion into silicon and the effect of heat treatment as considered by integrated circuit technology.

Keywords: Diffusion; Silicon; Integrated circuit; Interconnects
Received: 24 February 2021; **Revised:** 18 March 2021; **Accepted:** 25 March 2021

1. Introduction

One technology that applies solid-state diffusion is the fabrication of semiconductor integrated circuits (ICs). Each integrated circuit chip is a thin square wafer having dimensions on the order of 6 mm by 6 mm by 0.4 mm; furthermore, millions of interconnected electronic devices and circuits are embedded in one of the chip faces. Single-crystal silicon is the base material for most ICs. In order for these IC devices to function satisfactorily, very precise concentrations of an impurity (or impurities) must be incorporated into minute spatial regions in a very intricate and detailed pattern on the silicon chip; one way this is accomplished is by atomic diffusion.

Most practical diffusion situations are unsteady-state ones. That is, the diffusion flux and the concentration gradient at some particular point in a solid vary with time, with a net accumulation or depletion of the diffusing species resulting. This is illustrated in Fig. (1), which shows concentration profiles at three different diffusion times.

Normally two heat treatments are used in this process. In the first, or *predeposition step*, impurity atoms are diffused into the silicon, often from a gas phase, the partial pressure of which is maintained constant. Thus, the surface composition of the impurity also remains constant over time, such that impurity concentration within the silicon is a function of position and time according to Equation 5.5. Predeposition treatments are normally carried out within the temperature range of 900 and 1000°C and for times typically less than one hour.

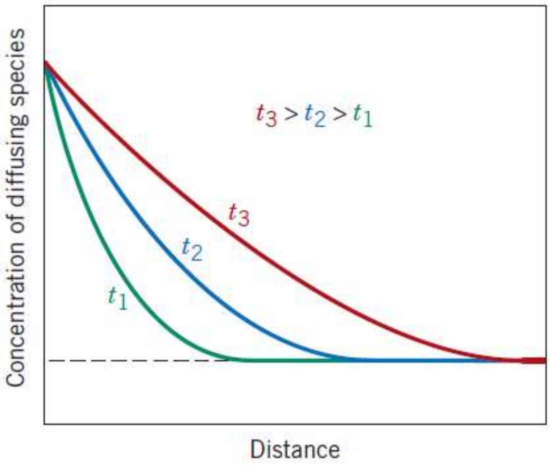

Fig. (1) Concentration profiles for unsteady-state diffusion taken at three different times, t_1, t_2, and t_3

The second treatment, sometimes called *drive-in diffusion*, is used to transport impurity atoms farther into the silicon in order to provide a more suitable concentration distribution without increasing the overall impurity content. This treatment is carried out at a higher temperature than the predeposition one (up to about 1200°C), and also in an oxidizing atmosphere so as to form an oxide layer on the surface. Diffusion rates through this SiO_2 layer are relatively slow, such that very few impurity atoms diffuse out of and escape from the silicon. Schematic concentration profiles taken at three different times for this diffusion situation are shown in Fig. (2); these profiles may be compared and contrasted to those in Fig. (1) for the case wherein the surface concentration of diffusing species is held constant. In addition, figure (3) compares (schematically) concentration profiles for predeposition and drive-in treatments.

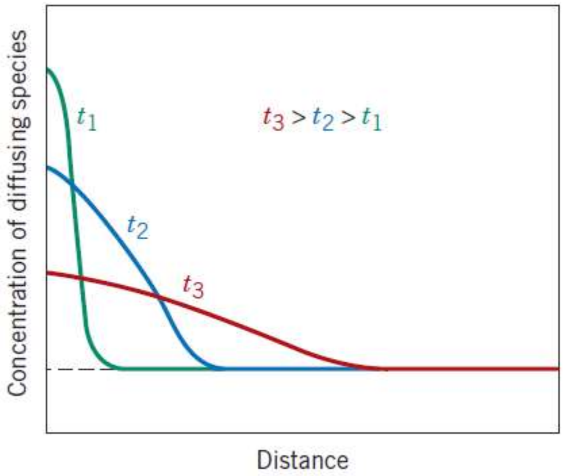

Fig. (2) Schematic concentration profiles for drive-in diffusion of semiconductors at three different times, t_1, t_2, and t_3

If we assume that the impurity atoms introduced during the predeposition treatment are confined to a very thin layer at the surface of the silicon (which, of course, is only an approximation), then the solution to Fick's second law takes the form

$$C(x,t) = \frac{Q_0}{\sqrt{\pi D t}} \exp\left(-\frac{x^2}{4Dt}\right) \qquad (1)$$

Here Q_0 represents the total amount of impurities in the solid that were introduced during the predeposition treatment (in number of impurity atoms per unit area); all other parameters in this equation have the same meanings as previously. Furthermore, it can be shown that

$$Q_0 = 2C_S\sqrt{\frac{D_p t_p}{\pi}} \qquad (2)$$

where C_s is the surface concentration for the predeposition step (Fig. 3), which was held constant, D_p is the diffusion coefficient, and t_p is the predeposition treatment time.

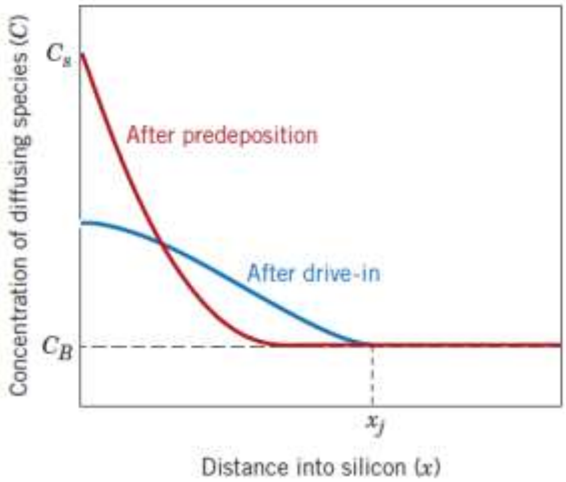

Fig. (3) Schematic concentration profiles taken after (1) predeposition and (2) drive-in diffusion treatments for semiconductors. Also shown is the junction depth, x_j

Another important diffusion parameter is *junction depth*, x_j. It represents the depth (i.e., value of x) at which the diffusing impurity concentration is just equal to the background concentration of that impurity in the silicon (C_B) (Fig. 3). For drive-in diffusion x_j may be computed using the following expression:

$$x_j = \left[(4D_d t_d) ln\left(\frac{Q_0}{C_B\sqrt{\pi D_d t_d}}\right)\right]^{\frac{1}{2}} \qquad (3)$$

Here D_d and t_d represent, respectively, the diffusion coefficient and time for the drive-in treatment.

2. Experimental Part

Subsequent to the predeposition and drive-in heat treatments just described, another important step in the IC fabrication process is the deposition of very thin and narrow conducting circuit paths to facilitate the passage of current from one device to another; these paths are called *interconnects*, and several are shown in Fig. (4), a scanning electron micrograph of an IC chip. Of course the material to be used for interconnects must have a high electrical conductivity – a metal, because, of all materials, metals have the highest conductivities. Table (1) cites values for silver, copper, gold, and aluminum, the most conductive metals. On the basis of these conductivities, and discounting material cost, Ag is the metal of choice, followed by Cu, Au, and Al.

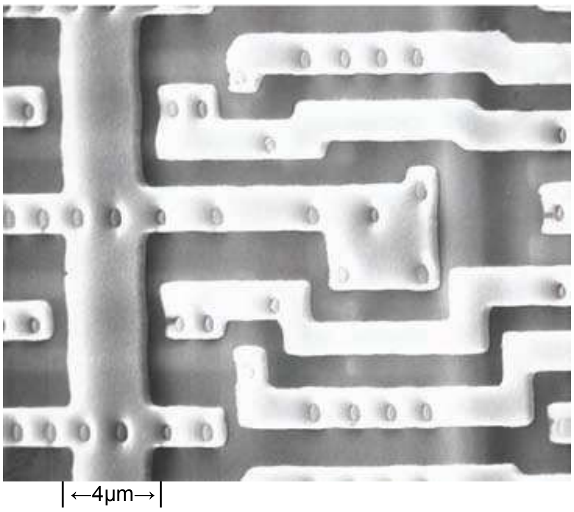

Fig. (4) Scanning electron micrograph of an integrated circuit chip, on which is noted aluminum interconnect regions. Approximately 2000X. (Photograph courtesy of National Semiconductor Corporation.)

Table (1) Room-Temperature Electrical Conductivity Values for Silver, Copper, Gold, and Aluminum (the Four Most Conductive Metals)

Metal	Electrical conductivity $(\Omega.m)^{-1}$ x10^7
Aluminum	3.8
Gold	4.3
Copper	6.0
Silver	6.8

Once these interconnects have been deposited, it is still necessary to subject the IC chip to other heat treatments, which may run as high as 500°C. If, during these treatments, there is significant diffusion of the interconnect metal into the silicon, the electrical functionality of the IC will be destroyed. Thus, because the extent of diffusion is dependent on the magnitude of the diffusion coefficient, it is necessary to select an interconnect metal that has a small value of *D* in silicon. Figure (5) plots the logarithm of *D* versus 1/*T* for the diffusion, into silicon, of copper, gold, silver, and aluminum. Also, a dashed vertical line has been constructed at 500°C, from which values of *D* for the four metals are noted at this temperature. Here it may be seen that the diffusion coefficient for aluminum in silicon ($2.5\text{x}10^{-21}$ m^2/s) is at least four orders of magnitude (i.e., a factor of 10^4) lower than the values for the other three metals.

Aluminum is indeed used for interconnects in some integrated circuits; even though its electrical conductivity is slightly lower than the values for silver, copper, and gold, its extremely low diffusion coefficient makes it the material of choice for this application.An aluminum–copper–silicon alloy (94.5 wt% Al-4 wt% Cu-1.5 wt% Si) is sometimes also used for interconnects; it not only bonds easily to the surface of the chip, but is also more corrosion resistant than pure aluminum.

More recently, copper interconnects have also been used. However, it is first necessary to deposit a very thin layer of tantalum or tantalum nitride beneath the copper, which acts as a barrier to deter diffusion of Cu into the silicon.

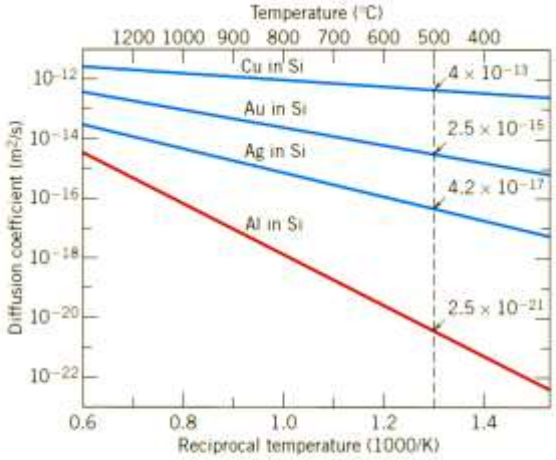

Fig. (5) Logarithm of *D*-versus-1/*T* (K) curves (lines) for the diffusion of copper, gold, silver, and aluminum in silicon. Also noted are *D* values at 500°C

3. Results and Discussion

Boron atoms are to be diffused into a silicon wafer using both predeposition and drive-in heat treatments; the background concentration of B in this silicon material is known to be $1\text{x}10^{20}$ atoms/m^3. The predeposition treatment is to be conducted at 900°C for 30 minutes; the surface concentration of B is to be maintained at a constant level of $3\text{x}10^{26}$ atoms/m3. Drive-in diffusion will be carried out at 1100°C for a period of 2 h. For the diffusion coefficient of B in Si, values of Q_d and D_0 are 3.87 eV/atom and $2.4\text{x}10^{-3}$ m^2/s, respectively.

The value of Q_0 is calculated using Eq. (2). However, before this is possible, it is first necessary to determine the value of *D* for the predeposition treatment [D_p at $T=T_p$ = 900°C (1173 K)] using Equation 5.8. (*Note:* For the gas constant *R* in Equation 5.8, we use Boltzmann's constant *k*, which has a value of $8.62\text{x}10^{-5}$ eV/atom.K). Thus

$$D_p = D_0 \exp\left(-\frac{Q_d}{k_B T_p}\right) \qquad (4)$$

$$= (2.4\times10^{-3}\mathrm{m}^2/\mathrm{s})\exp\left[-\frac{3.87\ \mathrm{eV/atom}}{(8.62\times10^{-5}\mathrm{eV/atom})(1173\mathrm{K})}\right]$$

$$= 5.73\times10^{-20}\mathrm{m}^2/s$$

The value of Q_0 may be determined according to Eq. (2) as follows:

$$Q_0 = 2C_S\sqrt{\frac{D_p t_p}{\pi}} \qquad (2)$$

$$= 2(3\times10^{26}\ \mathrm{atom/m^3})\sqrt{\frac{(5.73\times10^{-20}\ \mathrm{m^2/s})(30\ \mathrm{min})(60\ \mathrm{s/min})}{\pi}}$$

$$= 3.44\times10^{18}\ \mathrm{atom/m^2}$$

Computation of the junction depth requires that we use Eq. (3). However, before this is possible it is necessary to calculate *D* at the temperature of the drive-in treatment [D_d at 1100°C (1373 K)]. Thus,

$$D_d = (2.4\times10^{-3}\mathrm{m}^2/\mathrm{s})\exp\left[-\frac{3.87\ \mathrm{eV/atom}}{(8.62\times10^{-5}\mathrm{eV/atom})(1373\mathrm{K})}\right]$$

$$= 1.51\times10^{-17}\mathrm{m}^2/s$$

Now, from Eq. (3),

$$x_j = \left[(4D_d t_d)ln\left(\frac{Q_0}{C_B\sqrt{\pi D_d t_d}}\right)\right]^{\frac{1}{2}} \qquad (3)$$

$$= \left[4(1.51\times10^{-17})(7200)\right.$$

$$\left.\times\, ln\left(\frac{3.44\times10^{18}}{(1\times10^{20})\sqrt{(\pi)(1.51\times10^{-17})(7200)}}\right)\right]^{\frac{1}{2}}$$

$$= 2.19\times10^{-6}\ \mathrm{m} = 2.19\mu\mathrm{m}$$

At x=1 μm for the drive-in treatment, we compute the concentration of B atoms using Eq. (1) and values for Q_0 and D_d determined previously as follows:

$$C(x,t) = \frac{Q_0}{\sqrt{\pi D t}}\exp\left(-\frac{x^2}{4Dt}\right)$$

$$= \frac{3.44\times10^{18}}{\sqrt{(\pi)(1.51\times10^{-17})(7200)}}\exp\left(-\frac{(1\times10^{-6})^2}{(4)(1.51\times10^{-17})(7200)}\right)$$

$$= 5.90\times10^{23}\ \mathrm{atoms/m^3}$$

4. Conclusion

In this study, the concentration profiles for unsteady-state and drive-in diffusion conditions into semiconductors taken at different times were considered and compared. As well, the diffusion of copper, gold, silver, and aluminum in silicon was determined using the analytical expressions derived from Fick's law of diffusion. These situations were compared to the experimental situation of boron diffusion into silicon and the effect of heat treatment as considered by integrated circuit technology.

References

[1] M. Rudan, **"Physics of Semiconductor Devices"**, Springer (NY, 2015), Ch. 23, 545-546.

[2] M. Grundmann, **"The Physics of Semiconductors"**, Springer (NY, 2016), Ch. 8, 282-283.

[3] W.D. Callister Jr. and D.G. Rethwisch, **"Materials Science and Engineering: An Introduction"**, 8th ed., John Wiley & Sons, Inc. (2010), Ch. 5, 127-132.

[4] O.A. Hamadi, "Determination of chromium diffusivity in boron-doped silicon", *Almustansiriya J. Sci.*, 12(5) (2001) 247-253.

[5] O.A. Hamadi et al., "Ohmic characteristics of Ni/Si contact produced by laser-induced diffusion technique", *Almustansiriya J. Sci.*, 12(6) (2001) 475-483.

[6] O.A. Hamadi et al., "Heat-annealed enhanced-diffusion of silver in gallium arsenide", *J. Edu. Al-Mustansiriya Univ.*, 3 (2001) 35-44.

[7] O.A. Hamadi et al., "Effect of temperature on the electrical characteristics of Ni-Si structure", *Eng. Technol. J.*, 21(1) (2002) 1-8.

[8] O.A. Hamadi et al., "Characteristics of Cr diffusion in p-type silicon", *Eng. Technol. J.*, 21(2) (2002) 55-59.

[9] R.A. Ismail et al., "Characterization of Si p-n Photodetectors Produced by Laser-Induced Diffusion", *Inter. J. Mod. Phys.*, 19(31) (2005) 4619-4628.

[10] O.A. Hamadi, K.Z. Yahiya and O.N.S. Jassim, "Properties of Silicon Carbide Thin Films Deposited by Vacuum Thermal Evaporation", *J. of Semicond. Technol. Sci.*, 5(3) (2005) 182-186.

[11] O.A. Hamadi and K.Z. Yahiya, "Optical and electrical properties of selenium-antimony heterojunction formed on silicon substrate", *Sharjah Univ. J. Pure Appl. Sci.*, 4(2) (2007) 1-11.

[12] R.A. Ismail et al., "Full Characterization at 904nm of Si p-n Junction Photodetectors Produced by LID Technique", *Euro. Phys. J.: Appl. Phys.*, 38 (2007) 197-201.

[13] O.A. Hamadi et al., "Normalized Characteristics of Laser-Induced Diffusion of Arsenic Dopants in Silicon", *Eng. Technol. J.*, 27(4) (2007) 39-42.

[14] A.A.K. Hadi et al., "Optoelectronic Characteristics of As-doped Si Photodetectors Produced by LID Technique", *Iraqi J. Appl. Phys. Lett.*, 1(2) (2008) 23-26.

[15] O.A. Hamadi, "Effect of Annealing on the Electrical Characteristics of CdO-Si Heterostructure Produced by Plasma-Induced Bonding Technique", *Iraqi J. Appl. Phys.*, 4(3) (2008) 34-37.

[16] A.K. Yousif et al., "Plasma-Induced Etching of Silicon Surfaces", *Bulg. J. Phys.*, 35(3) (2008) 191-197.

[17] O.A. Hamadi, "Characteristics of CdO-Si Heterostructure Produced by Plasma-Induced Bonding Technique", *Proc. IMechE, Part L, J. Mater.: Design and Applications*, 222 (2008) 65-71, DOI: 10.1243/14644207JMDA56.

[18] O.A. Hamadi, "Profiling of Antimony Diffusivity in Silicon Substrates using Laser-Induced Diffusion Technique", *Iraqi J. Appl. Phys. Lett.*, 3(1) (2010) 23-26.

[19] O.A. Hammadi, "Photovoltaic Properties of Thermally-Grown Selenium-Doped Silicon Photodiodes for Infrared Detection Applications", *Phot. Sens.*, 5(2) (2015) 152-158, DOI: 10.1007/s13320-015-0241-4

[20] O.A. Hammadi et al., "Fabrication of UV Photodetector from Nickel Oxide Nanoparticles Deposited on Silicon Substrate by Closed-Field Unbalanced Dual Magnetron Sputtering Techniques", *Opt. Quantum Electron.*, 47(12) (2015) 3805-3813, DOI: 10.1007/s11082-015-0247-6.

[21] O.A. Hammadi and N.E. Naji, "Electrical and spectral characterization of CdS/Si heterojunction prepared by plasma-induced bonding", *Opt. Quantum Electron.*, 48(8) (2016) 375-381, DOI: 10.1007/s11082-016-0647-2

[22] O.A. Hammadi, "Characteristics of Heat-Annealed Silicon Homojunction Infrared Photodetector Fabricated by Plasma-Assisted Technique ", *Phot. Sens.*, 6(4) (2016) 345-350, DOI: 10.1007/s13320-016-0338-4

[23] O.A. Hamadi, "Characterization of SiC/Si Heterojunction Fabricated by Plasma-Induced Growth of Nanostructured Silicon Carbide Layer on Silicon Surface", *Iraqi J. Appl. Phys.*, 12(2) (2016) 9-13.

IRAQI JOURNAL OF APPLIED PHYSICS
Vol. 17, No. 1, January-March 2021, pp. 25-28

Effective Collection and Transformation of Emission into Directional Radiation Based on Surface Plasmon-Coupled Emission

Ahmed A. Sadoon[1]
Rahim S. Kashif[2]
Ranaswami Shutra[2]

[1] *Department of Physics,*
College of Science,
University of Wasit,
Kut, IRAQ
[2] *School of Applied Sciences,*
National University of Bangalore,
Bangalore, INDIA

The use of metallic particles to modify emission was accomplished by interaction of the excited dipoles of the fluorophore with oscillating electrons in a nearby metallic surface. We used the term "metal" to describe such surfaces. We described how a fluorophore near a metal can have a different radiative-decay rate. This is an unusual effect because this rate does not change substantially when a fluorophore is in different environments. In this study, we describe another phenomenon that occurs when a fluorophore is near a metal. Under certain circumstances a fluorophore can couple with a continuous metallic surface to create groups of oscillating electrons called surface plasmons. If the metal film is thin and on an appropriate substrate the plasmons radiate their energy into the substrate. We call this phenomenon surface plasmon coupled emission (SPCE). There are numerous potential applications for this phenomenon that efficiently collects the emission and transforms it into directional radiation.

Keywords: Directional radiation; Surface plasmon; Plasmon-coupled emission; Fluorescence
Received: 25 February 2021; **Revised:** 14 March 2021; **Accepted:** 21 March 2021

1. Introduction

Prior to describing the theory for SPCE it is informative to describe this phenomenon (Fig. 1). Suppose an excited fluorophore is positioned above a thin silver film, where the metal film is continuous and about 50 nm thick. Such films are visually opaque. Remarkably, the emission from the fluorophore is not reflected but is efficiently transferred through the film. The spatial distribution of fluorescence is isotropic or nearly isotropic. However, the emission seen through the film occurs only at a unique angle θ_F measured from the normal. Since the sample is symmetric about the normal *z*-axis the emission occurs as a cone around the axis. This cone is not due to selective transmission of emission through the film. A large fraction of the total emission appears in the cone. About half of the emission appears in the cone and about half is free-space emission away from the film. The emission in the cone has the same emission spectrum as the fluorophore.

The light from the excited fluorophore appearing in the cone is called surface plasmon-coupled emission (SPCE) [1]. This name reflects our current understanding of the phenomenon. We believe the excited fluorophore creates surface plasmons in the metal. These plasmons do not appear to be the result of RET to the surface because the distances over which SPCE occurs are too large for RET. SPCE occurs over distances up to 200 nm or 2000Å, which are much larger than Förster distances near 50Å. The plasmons radiate into the substrate at an angle determined by the optical properties of the metal and substrate. Since the wavelength distribution of SPCE is the same as the fluorophore emission it is tempting to assume it originates from the fluorophore. However, the emission is 100% p-polarized, even if the fluorophores are randomly oriented and excited with unpolarized light. See Chapter 2 for a definition of p-polarization. This polarization indicates the surface plasmons are radiating and not the fluorophores.

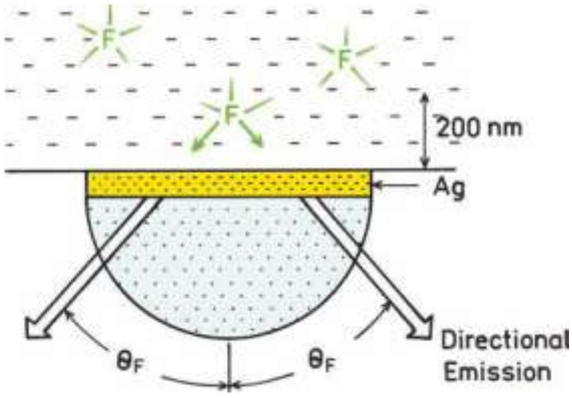

Fig. (1) Surface plasmon-coupled emission. F is a fluorophore

The phenomenon of SPCE appears to be closely related to surface-plasmon resonance (SPR). SPR is now widely used in the biosciences and provides a generic approach to measurement of biomolecule interactions on surfaces [2-6]. A schematic description of SPR is shown in Fig. (2). The measurement is based on the interaction of light with thin metal films on a glass substrate. The film is typically made of gold 40–50 nm thick. The surface contains a capture biomolecule that has affinity for the analyte of interest. The capture biomolecule is typically covalently bound to the gold surface. This sample is optically coupled to a hemispherical or hemicylindrical prism by an index-matching fluid. Light impinges on the gold film through the prism, which is called the Kretschmann configuration. The instrument measures the reflectivity of the gold film at various angles of incidence (θ), with the same angle used for observation (θ).

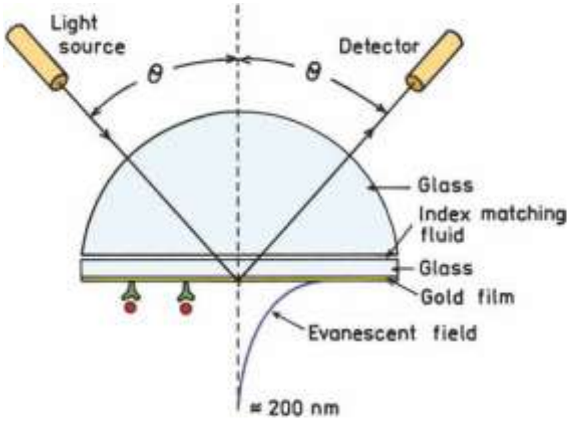

Fig. (2) Typical configuration for surface-plasmon resonance analysis. The incident beam is p-polarized

2. Approach and Modelling

The usefulness of SPR is due to the dependence of the reflectivity of the gold film on the refractive index of the solution immediately above the gold film. The angle-dependent reflectivity of the gold surface is dependent on the refractive index of the solution because there is an evanescent field extending from the gold surface into the solution. Binding of macromolecules above the gold film causes small changes in the refractive index, which result in changes in reflectivity. Figure (3) shows typical SPR data: a plot of reflectivity versus the angle of incidence for a 47-nm gold film [7-9]. The reflectivity minimum occurs at the SPR angle. The SPR angles change as the gold surface is coated with 11-mercaptoundecanoic acid (MU), then biotinylated polylysine (PL), and finally avidin. The changes in SPR angle are due to changes in the refractive index near the gold surface due to the adsorbed layers.

The decrease in reflectivity at the SPR angle (θ_{SP}) is due to absorption of the incident light at this particular angle of incidence. At this angle the incident light is absorbed and excites electron oscillations on the metal surface. The reflectivity is sensitive to the refractive index because of the evanescent field that penetrates approximately 200 nm into the solution (Fig. 2). The evanescent field appears whenever there is resonance between the incident beam and the gold surface. An evanescent field is not present when there is no plasmon resonance, that is, when the reflectivity is high.

The existence of an evanescent field is reminiscent of total internal reflectance (TIR), which occurs between a glass–water interface when the angle of incidence from the glass slide exceeds the critical angle [10]. There can be confusion about the relationship between the critical angle in TIR (θ_C) and the SPR angle (θ_{SP}). The physical origins of θ_C and θ_{SP} are similar, in that both are dependent on wavevector matching at the sample–glass or metal interface. However, these angles are different and not directly related. This difference between θ_C and θ_{SP} is illustrated in Fig. (4), which compares glass and silver–coated glass surfaces [11,12]. The silver-coated surface shows high reflectivity at all angles except around the plasmon angle near 30°. The reflectivity of a glass surface is quite different. The reflectivity is low below the critical angle θ_C, increases sharply to nearly 100% at θ_C, and remains high for all angles above θ_C. For the glass surface and angles above θ_C there exists an evanescent field from the totally internally reflected light. For the silver-coated glass there is no evanescent field in the aqueous phase unless the angle of incidence is near the SPR angle. The reflectivity of the silver film is high at angles significantly larger or smaller than θ_{SP}.

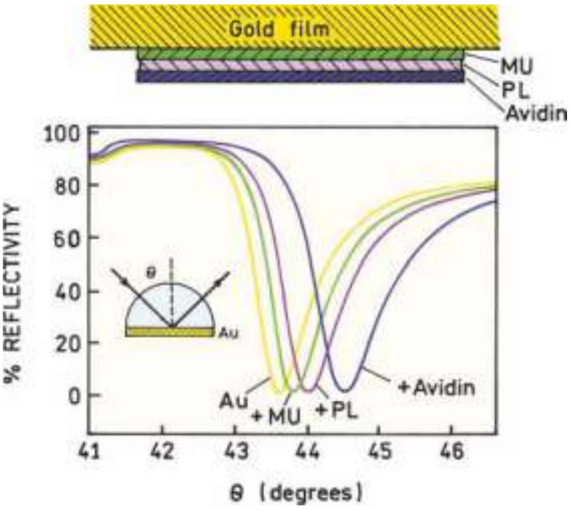

Fig. (3) SPR reflectivity curves for a 47-nm gold film on BK-7 glass. Illumination was at 633 nm. The gold film was progressively coated with 11-mercaptoundecanoic acid (MU), followed by biotinylated poly-lysine (PL), and then avidin. Adapted from [7–9]

The evanescent wave due to SPR is much more intense than that due to TIR [11-17]. The relative strengths of the fields can be measured by the fluorescence from fluorophores near the surface. For the sample shown in Fig. (4) fluorophores were localized within the evanescent field by coating with a polyvinyl alcohol (PVA) film that contained a fluorophore. The dependence of the emission on the incident angle indicates the relative intensity of the evanescent wave felt by the fluorophores. For the glass surface the emission intensity is low for $\theta < \theta_C$. This low value is essentially the same as seen in a typical fluorescence measurement where the fluorophore is excited in a glass or quartz cuvette. As the incident angle exceeds θ_C the intensity drops about twofold because the incident light undergoes TIR rather than passing into the sample. Above the critical angle the remaining intensity represents the amount of excitation due to the TIR evanescent wave. This result indicates that the field strength for TIR is roughly the same for the incident light and the evanescent wave.

3. Results and Discussion

Different results are seen for the labeled film on the silver surface. The emission intensity is near zero for angles above and below θ_C because of the high reflectivity of the metal film. In contrast to uncoated glass, the light does not penetrate the sample even though $\theta < \theta_C$. There is a dramatic increase in the emission intensity of the film near the plasmon angle: about 15-fold. This effect is due to a 10- to 40-fold increase in the intensity of the evanescent field above silver as compared to above glass with TIR [18-21]. This increase in field strength above a metal film is one origin of the increased sensitivity possible with plasmon-coupled emission.

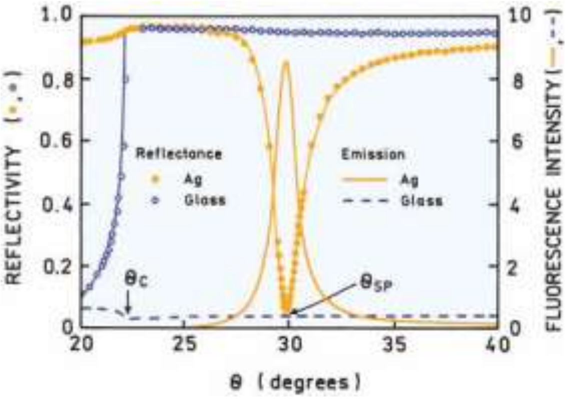

Fig. (4) Reflectivity curves for a bare glass and silver-coated glass, both spin coated with a fluorophore in polyvinyl alcohol. The prism is $LaSFN_9$ glass, 633 nm. Also shown is the fluorescence from the labeled PVA film on the glass and silver surfaces [11]

An important characteristic of the SPR angles is that they are strongly dependent on wavelength. Fig. (5) shows the reflectivity curves of a gold film for several wavelengths [22]. The surface plasmon angle decreases as the wavelength decreases. The dependence on wavelength can be understood in terms of the optical constants of the metals, which depend upon wavelength (frequency) and the dielectric constant of the adjacent prism. This dependence of θ_{SP} on wavelength is the origin of intrinsic spectral resolution when observing surface plasmon-coupled emission.

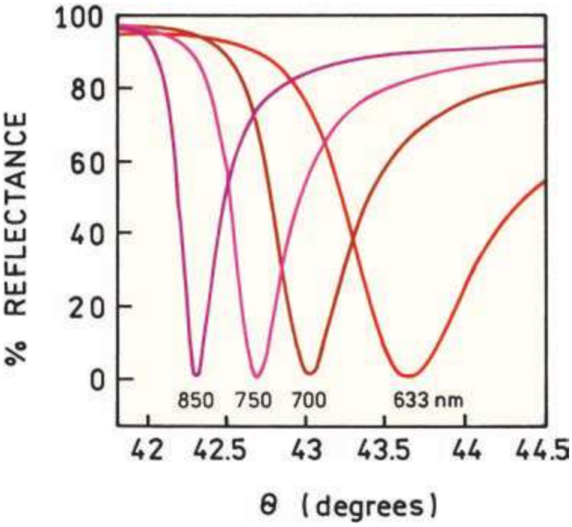

Fig. (5) Calculated wavelength-dependent reflectivity for a 47-nm-thick gold film [22]

4. Conclusion

In this study, we describe another phenomenon that occurs when a fluorophore is near a metal. Under certain circumstances a fluorophore can couple with a continuous metallic surface to create groups of oscillating electrons called surface plasmons. If the metal film is thin and on an appropriate substrate the plasmons radiate their energy into the substrate. We call this phenomenon surface plasmon coupled emission (SPCE). There are numerous potential applications for this phenomenon that efficiently collects the emission and transforms it into directional radiation.

References

[1] J.R. Lakowicz, “Radiative decay engineering, 3: surface plasmon-coupled directional emission”, *Anal. Biochem.*, 324 (2004) 153-169.

[2] Z. Salamon, H.A. Macleod and G. Tollin, “Surface plasmon resonance spectroscopy as a tool for investigating the biochemical and biophysical properties of membrane protein systems, I: theoretical principles”, *Biochim. Biophys. Acta*, 1331 (1997) 117-129.

[3] J. Melendez, R. Carr, D.U. Bartholomew, K. Kukanskis, J. Elkind, S. Yee, C. Furlong and R. Woodbury, “A commercial solution for surface plasmon sensing”, *Sensors and Actuators B*, 35-36 (1996) 212-216.

[4] B. Liedberg and I. Lundstrom, “Principles of biosensing with an extended coupling matrix and surface plasmon resonance”, *Sensors and Actuators B*, 11 (1993) 63-72.

[5] M.A. Cooper, “Optical biosensors in drug discovery”, *Nature Rev.*, 1 (2002) 515-528.

[6] G.J. Wegner, H.J. Lee and R.M. Corn, “Characterization and optimization of peptide

arrays for the study of epitope–antibody interactions using surface plasmon resonance imaging", *Anal. Chem.,* 74 (2002) 5161-5168.

[7] A.G. Frutos and R.M. Corn, "SPR of ultrathin organic films", *Anal. Chem.,* 70 (1998) 449A-455A.

[8] C.E. Jordan, B.L. Frey, S. Kornguth and R.M. Corn, "Characterization of Poly-L-lysine adsorption onto alkanethiol-modified gold surfaces with polarization-modulation Fourier transform infrared spectroscopy and surface plasmon resonance measurements", *Langmuir,* 10 (1994) 3642-3648.

[9] B.L. Frey, C.E. Jordan, S. Kornguth and R.M. Corn, "Control of the specific adsorption of proteins onto gold surfaces with poly(l-ysine) monolayers", *Anal. Chem.,* 67 (1995) 4452-4457.

[10] D. Axelrod, E.H. Hellen and R.M. Fulbright, "Total internal reflection fluorescence", in *Topics in fluorescence spectroscopy*, Vol 3: *Biochemical applications*, pp. 289–343. ed JR Lakowicz. Plenum Press (NY, 1992).

[11] T. Neumann, M.L. Johansson, D. Kambhampati and W. Knoll, "Surface-plasmon fluorescence spectroscopy", *Adv. Funct. Mater.,* 12(9) (2002) 575-586.

[12] T. Liebermann and W. Knoll, "Surface-plasmon field-enhanced fluorescence spectroscopy", *Colloids Surf.,* 171 (2000) 115-130.

[13] S. Ekgasit, G. Stengel and W. Knoll, "Concentration of dye-labeled nucleotides incorporated into DNA determined by surface plasmon resonance-surface plasmon fluorescence spectroscopy", *Anal. Chem.,* 76 (2004) 4747-4755.

[14] S. Ekgasit, C. Thammacharoen, F. Yu and W. Knoll, 2004. "Evanescent field in surface plasmon resonance and surface plasmon field-enhanced fluorescence spectroscopies", *Anal. Chem.,* 76 (2004) 2210-2219.

[15] S. Roy, J.-H. Kim, J.T. Kellis, A.J. Poulose, C.R. Robertson and A.P. Gast, "Surface plasmon resonance/surface plasmon enhanced fluorescence: an optical technique for the detection of multicomponent macromolecular adsorption at the solid/liquid interface", *Langmuir*, 18 (2002) 6319-6323.

[16] H. Yokota, K. Saito and T. Yanagida, "Single molecule imaging of fluorescently labeled proteins on metal by surface plasmons in aqueous solution", *Phys. Rev. Lett.,* 80(20) (1998) 4606-4609.

[17] F. Yu, B. Persson, S. Löfås and W. Knoll, 2004. "Attomolar sensitivity in bioassays based on surface plasmon fluorescence spectroscopy", *J. Am. Chem. Soc.,* 126 (2004) 8902-8903.

[18] J.W. Attridge, P.B. Daniels, J.K. Deacon, G.A. Robinson and G.P. Davidson, "Sensitivity enhancement of optical immunosensors by the use of a surface plasmon resonance fluoroimmunoassay", *Biosens. Bioelectron.,* 6 (1991) 201-214.

[19] T. Liebermann, W. Knoll, P. Sluka and R. Herrmann, "Complement hybridization from solution to surface-attached probe-oligonucleotides observed by surface-plasmon-field-enhanced fluorescence spectroscopy", *Colloids Surf.,* 169 (2000) 337-350.

[20] N. Fukuda, M. Mitsuishi, A. Aoki and T. Miyashita, "Photocurrent enhancement for polymer Langmuir–Blodgett monolayers containing ruthenium complex by surface plasmon resonance", *J. Phys. Chem. B,* 106 (2002) 7048-7052.

[21] G. Stengel and W. Knoll, "Surface plasmon field-enhanced fluorescence spectroscopy studies of primer extension reactions", *Nucleic Acids Res.,* 33(7) (2005) e69.

[22] M.J. Natan and L.A. Lyon, "Surface plasmon resonance biosensing with colloidal Au amplification", in *Metal nanoparticles: synthesis, characterization, and applications*, pp. 183-205. ed. DL Feldheim, CA Foss. Marcel Dekker (NY, 2002).

IRAQI JOURNAL OF APPLIED PHYSICS
Vol. 17, No. 1, January-March 2021, pp. 29-32

Sameer A. Mohammed
Enad S. Kadhim
Rasool M. Alwan

Department of Mechanical Engineering,
College of Engineering,
University of Najaf,
Najaf, IRAQ

Temporally and Spatially Localized Phase Transformations in Ferrous Alloys for Materials Processing Applications

In this study, the temporally and spatially localized phase transformations in ferrous alloys were investigated. These transformations were temporally restricted by rapid irradiation with laser pulses and quenching by liquid nitrogen jet flow. The spatial localization of these phase transformations was carried out by placing the sample of ferrous alloy between two thermal and electrical insulators to prevent any heat or charge flow towards the surrounding. The optical microscopy was used for introducing the microstructures of the ferrous alloy samples. It was shown that the temporal and spatial localization can enhance the eutectic and eutectoid positions on the iron-carbon phase diagrams to which the ferrous alloy are classified.

Keywords: Phase transformation; Ferrous alloys; Cast iron; Heat treatment
Received: 28 February 2021; **Revised:** 19 March 2021; **Accepted:** 26 March 2021

1. Introduction

Generically, cast irons are a class of ferrous alloys with carbon contents above 2.14 wt%; in practice, however, most cast irons contain between 3.0 and 4.5 wt% C and, in addition, other alloying elements. A reexamination of the iron–iron carbide phase diagram (Fig. 1) reveals that alloys within this composition range become completely liquid at temperatures between approximately 1150 and 1300°C, which is considerably lower than for steels [1,2]. Thus, they are easily melted and amenable to casting. Furthermore, some cast irons are very brittle, and casting is the most convenient fabrication technique [3].

Cementite (Fe_3C) is a metastable compound, and under some circumstances it can be made to dissociate or decompose to form α-ferrite and graphite, according to the reaction [4]

$$Fe_3C \rightarrow 3Fe\ (\alpha) + C\ (graphite) \qquad (1)$$

Thus, the true equilibrium diagram for iron and carbon is not that presented in Fig. (1), but rather as shown in Fig. (2). The two diagrams are virtually identical on the iron-rich side (e.g., eutectic and eutectoid temperatures for the Fe–Fe_3C system are 1147 and 727°C, respectively, as compared to 1153 and 740°C for Fe–C); however, figure (2) extends to 100 wt% C such that graphite is the carbon-rich phase, instead of cementite at 6.7 wt% C (Fig. 1) [4,5]

This tendency to form graphite is regulated by the composition and rate of cooling. Graphite formation is promoted by the presence of silicon in concentrations greater than about 1 wt%. Also, slower cooling rates during solidification favor graphitization (the formation of graphite) [6]. For most cast irons, the carbon exists as graphite, and both microstructure and mechanical behavior depend on composition and heat treatment. The most common cast iron types are gray, nodular, white, malleable, and compacted graphite [7-10].

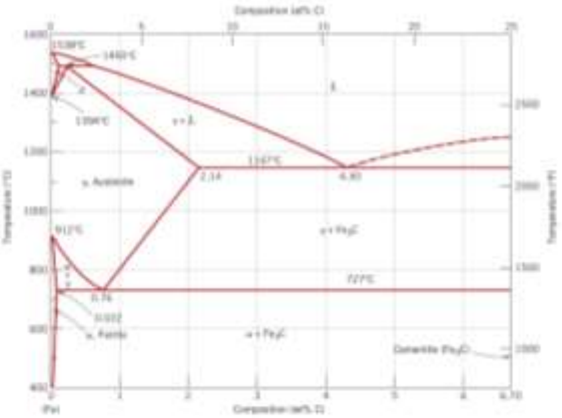

Figure 9.24 **Fig. (1) The iron–iron carbide phase diagram [5]**

The carbon and silicon contents of gray cast irons vary between 2.5 and 4.0 wt% and 1.0 and 3.0 wt%, respectively. For most of these cast irons, the graphite exists in the form of flakes (similar to corn flakes), which are normally surrounded by an α-ferrite or pearlite matrix; the microstructure of a typical gray iron is shown in Fig. (3a). Because of these graphite flakes, a fractured surface takes on a gray appearance, hence its name.

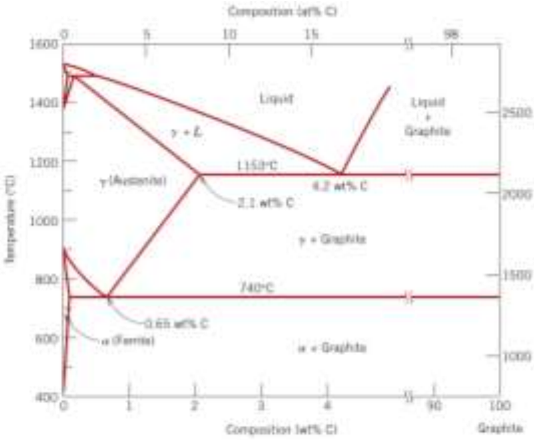

Fig. (2) The true equilibrium iron–carbon phase diagram with graphite instead of cementite as a stable phase [5]

Mechanically, gray iron is comparatively weak and brittle in tension as a consequence of its microstructure; the tips of the graphite flakes are sharp and pointed and may serve as points of stress concentration when an external tensile stress is applied. Strength and ductility are much higher under compressive loads. Gray irons do have some desirable characteristics and are utilized extensively. They are very effective in damping vibrational energy; this is represented in Fig. (4), which compares the relative damping capacities of steel and gray iron. Base structures for machines and heavy equipment that are exposed to vibrations are frequently constructed of this material. In addition, gray irons exhibit a high resistance to wear. Furthermore, in the molten state they have a high fluidity at casting temperature, which permits casting pieces that have intricate shapes; also, casting shrinkage is low. Finally, and perhaps most important, gray cast irons are among the least expensive of all metallic materials.

(a)

(b)

(c)

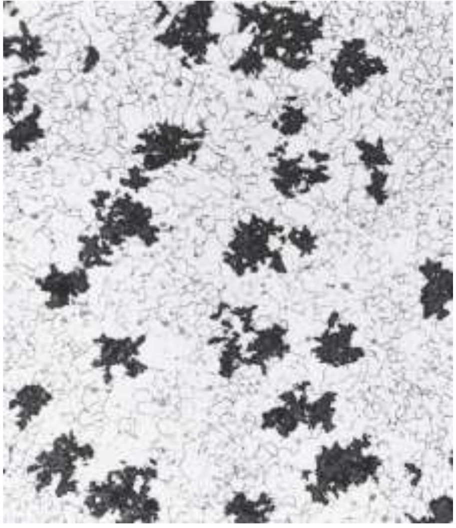

(d)

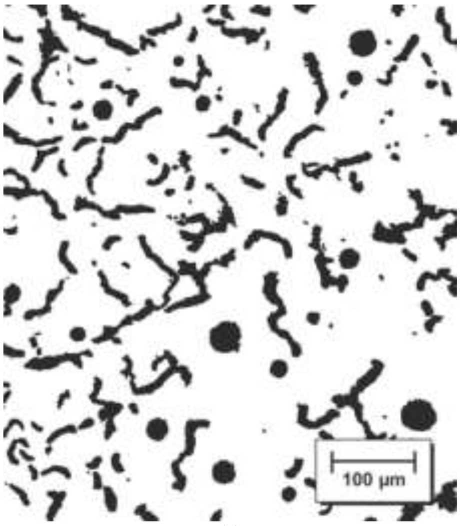

(e)

Fig. (3) Optical photomicrographs of various cast irons. (*a*) Gray iron: the dark graphite flakes are embedded in an *α*-ferrite matrix. 500µ. (*b*) Nodular (ductile) iron: the dark graphite nodules are surrounded by an *α*-ferrite matrix. 200µ. (*c*) White iron: the light cementite regions are surrounded by pearlite, which has the ferrite–cementite layered structure. 400µ. (*d*) Malleable iron: dark graphite rosettes (temper carbon) in an *α*-ferrite matrix. 150µ. (*e*) Compacted graphite iron: dark graphite wormlike particles are embedded within an *α*-ferrite matrix. 100µ [11]

Gray irons having microstructures different from that shown in Fig. (3a) may be generated by adjustment of composition and/or by using an appropriate treatment. For example, lowering the silicon content or increasing the cooling rate may prevent the complete dissociation of cementite to form graphite (Eq. 1) [12-14]. Under these circumstances the microstructure consists of graphite flakes embedded in a pearlite matrix. Figure (5) compares schematically the several cast iron microstructures obtained by varying the composition and heat treatment [15,16].

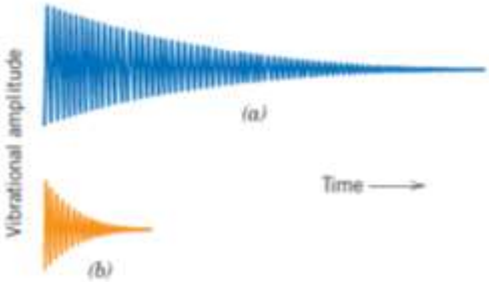

Fig. (4) Comparison of the relative vibrational damping capacities of (*a*) steel and (*b*) gray cast iron [15]

Adding a small amount of magnesium and/or cerium to the gray iron before casting produces a distinctly different microstructure and set of mechanical properties [17-19]. Graphite still forms, but as nodules or spherelike particles instead of flakes. The resulting alloy is called ductile or nodular iron, and a typical microstructure is shown in Fig. (3b). The matrix phase surrounding these particles is either pearlite or ferrite, depending on heat treatment (Fig. 5); it is normally pearlite for an as cast piece. However, a heat treatment for several hours at about 700°C will yield a ferrite matrix as in this photomicrograph. Castings are stronger and much more ductile than gray iron. In fact, ductile iron has mechanical characteristics approaching those of steel. For example, ferritic ductile irons have tensile strengths ranging between 380 and 480 MPa (55,000 and 70,000 psi), and ductilities (as percent elongation) from 10% to 20% [20-22]. Typical applications for this material include valves, pump bodies, crankshafts, gears, and other automotive and machine components.

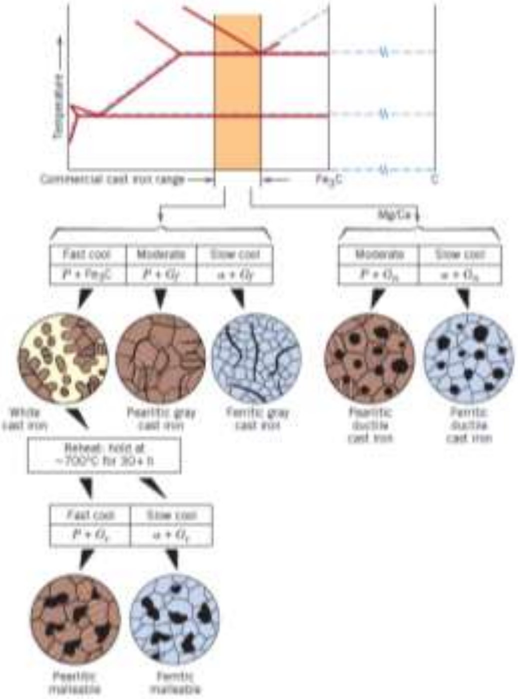

Fig. (5) From the iron–carbon phase diagram, composition ranges for commercial cast irons. Also shown are schematic microstructures that result from a variety of heat treatments. *Gf*, flake graphite; *Gr*, graphite rosettes; *Gn*, graphite nodules; *P*, pearlite; *α*, ferrite [23]

For low-silicon cast irons (containing less than 1.0 wt% Si) and rapid cooling rates, most of the carbon exists as cementite instead of graphite, as indicated in Fig. (5). A fracture surface of this alloy has a white appearance, and thus it is termed white cast iron [1]. An optical photomicrograph showing the microstructure of white iron is presented in Fig. (3c). Thick sections may have only a surface layer of white iron that was “chilled” during the casting process; gray iron forms at interior regions, which cool more slowly [24]. As a consequence of large amounts of the cementite phase, white iron is extremely hard but also very brittle, to the point of being virtually unmachinable. Its use is limited to applications that necessitate a very hard and wear-resistant surface, without a high degree of ductility—for example, as rollers in rolling mills [25-28]. Generally, white iron is used as an intermediary in the production of yet another cast iron, malleable iron [1].

References

[1] B. Bhushan (Ed.), **"Springer Handbook of Nanotechnology"**, Springer (2004), p. 27, 151, 438.

[2] M. Ohring, **"The Materials Science of Thin Films"**, Academic Press (San Diego) (1992), p. 79, 112, 182.

[3] N. Maluf and K. Williams, **"An Introduction to Microelectromechanical Systems Engineering"**, Artech House, Inc. (2004), p. 19, 39.

[4] W.D. Callister Jr. and D.G. Rethwisch, **"Materials Science and Engineering: An Introduction"**, 8th ed., John-Wiley & Sons, Ltd. (NY, 2010), p. 399.

[5] B. Massalski (Editor-in-Chief), **"Binary Alloy Phase Diagrams"**, 2nd ed., vol. 1, ASM International (OH, 1990).

[6] M.A. Lieberman and A.J. Lichtenberg, **"Principles of Plasma Physics and Materials Processing"**, 2nd ed., Wiley (2005), p. 535, 547.

[7] P.M. Martin, **"Handbook of Thin Film Deposition Techniques"**, Elsevier (2010), p. 4.

[8] P.M. Martin, **"Introduction to Surface Engineering and Functionally Engineered Materials"**, John Wiley & Sons, Inc. (2011), pp. 262-264, p. 339.

[9] B. Shah, Deposition of Tantalum on Steel by Sputtering, MSc thesis, New Jersey Institute of Technology (2001), p. 3, 15, 30.

[10] J.C. da Conceição Lorenzzi, "Boron nitride thin films deposited by magnetron sputtering on Si_3N_4", PhD thesis, Universidade de Aveiro, Departamento de Engenharia Cerâmica e do Vidro, pp. 10-16 (2007).

[11] Figures (a) and (b) courtesy of C. H. Brady and L. C. Smith, National Bureau of Standards, Washington, DC (now the National Institute of Standards and Technology, Gaithersburg, MD). Figure (c) courtesy of Amcast Industrial Corporation. Figure (d) reprinted with permission of the Iron Castings Society, Des Plaines, IL. Figure (e) courtesy of SinterCast, Ltd.

[12] C. O'Leary, Design, Construction and Characterisation of a Variable Balance Magnetron Sputtering System, Dublin City University, Ireland, p. 15 (1999).

[13] D. Huy Trinh, Nanocrystalline Alumina-Zirconia Thin Films Grown by Magnetron Sputtering, Linköping University, Sweden, (2008) p. 1.

[14] D.R. Gibson, "Deposition of multilayer optical coatings using closed field magnetron sputtering", online article (2006).

[15] Metals Engineering Quarterly, February 1961. Copyright 1961 American Society for Metals.

[16] E.C. Paloura, J. Lagowski and H.C. Gatos, "Growth and electronic properties of thin Si_3N_4 films grown on Si in a nitrogen glow discharge", J. Appl. Phys., 69, 3995-4002 (1991).

[17] F. Ghaleb and A. Belasri, "Numerical and theoretical calculation of breakdown voltage in the electrical discharge", Radiation Effects and Defects in Solids, 1 (2012) 1-7.

[18] H. Lorentz et al., "Characterization of low temperature SiO_2 and Si_3N_4 films deposited by plasma enhanced evaporation", J. Vac. Sci. Technol. B, 9, 208-214 (1991).

[19] H.B. Nie, Thin Film Deposition and Characterization, National University of Singapore (NUS) (2014).

[20] K. Deenamma Vargheese and G. Mohan Rao, "Ion-assisted deposition of silicon nitride films using electron cyclotron resonance plasma", J. Vac. Sci. Technol. A: Vac. Surf. Films. 19(4), 1336-1340 (2001).

[21] K. Tanabashi and K. Kobayashi, "Properties of vapor deposited silicon nitride films with varying excess Si content", Jpn. J. Appl. Phys., 12, 641-646 (1973).

[22] M. Julfikar Haider, Deposition of Hard and Solid Lubricant ($TiN+MoS_x$) Coating by Closed-Field Magnetron Sputtering, PhD thesis, Dublin University, Ireland (2005), pp. 56-58, 176.

[23] W. G. Moffatt, G.W. Pearsall and J. Wulff, **"The Structure and Properties of Materials"**, Vol. I, Structure, John Wiley & Sons (NY, 1964), p. 195.

[24] K. Wasa, M. Kitabatake, H. Adachi, **"Thin Film Materials Technology: Sputtering of Compound Materials"**, William Andrew Inc., p. 139, 116, 2, 119, 72, 106, 103, 9 (2004).

[25] S.V. Deshpande et al., "Optical properties of silicon nitride films deposited by hot filament chemical vapor deposition" J. Appl. Phys., 77(12), 6534-6541 (1995).

[26] S.W. et al., "Properties of plasma-enhanced chemical-vapor-deposited a-SiN_x:H by various dilution gases", J. Appl. Phys., 76, 3645-3655 (1994).

[27] S.M. Sze, "Current transport and maximum dielectric strength of silicon nitride films", J. Appl. Phys., 38, 2951-2955 (1967).

[28] T.E. Cook Jr. et al., "Band offset measurements of the Si_3N_4/GaN (0001) interface", J. Appl. Phys., 94(6), 3949-3954 (2003).

IRAQI JOURNAL OF APPLIED PHYSICS
Vol. 17, No. 1, January-March 2021, pp. 33-38

Shahid S. Kamar
Hussein V. Amirov
Hamid R. Hashimi
Mansour H. Arsatov

Department of Chemistry,
College of Applied Sciences,
Azerbaijan Technology University,
Ganja, AZERBAIJAN

Incorporation of Gold Nanoparticles in Single-Atomic Layered Materials and Their Plasmonic Absorption Characteristics as Highly-Efficient Nonlinear Optical Media

In this work, gold nanoparticles were incorporated in single-atomic layered materials by cold press at room temperature. These nanoparticles were dispersed in different solvents in order to introduce the effect of solvent type on their characteristics. The linear and nonlinear optical properties of the gold nanoparticles and prepared composite samples as well as their structural characteristics were determined. The linear optical activity of gold nanoparticles incorporated in the single-atomic layered material was highly damped while their nonlinear optical activity was affected but still observed. These results can be successfully used for the employment of precious metal nanoparticles in biomedical applications.

Keywords: Nonlinear optics; Gold nanoparticles; Atomic layered materials; Nanotechnology
Received: 20 February 2021; **Revised:** 18 March 2021; **Accepted:** 25 March 2021

1. Introduction

Nanotechnology has been rapidly growing and finding various applications in different fields of science and technology over the last decades. Different kinds of nanomaterials have been synthesized and characterized for their potential use in electrical, optical and medical devices and etc. The carbon allotropes discovered in recent decades, are the most outstanding examples of nanomaterials with distinct types of morphologies and applications. Fullerenes, carbon nanotubes, graphene and carbon nanoparticles are respectively 0, 1, 2 and 3 dimensional structures of carbon with their own characteristic physical properties. These carbon allotropes have been extensively studied for their mechanical, electrical, optical and nonlinear optical (NLO) properties. Concerning their NLO properties, it is shown that fullerenes have reverse saturable absorption at certain wavelengths [1,2], carbon nanotubes show ultrafast third-order nonlinearities and saturable absorption [3] and graphene shows ultrabroadband resonant NLO response [4,5]. Furthermore, it is shown that the recently discovered graphene oxide (GO) has reverse saturable absorption [6] and optical limiting properties [7-10].

A variety of techniques are being used for measuring the NLO properties of materials. Among them, the z-scan technique introduced by Sheik-Bahae et al. [11,12] is considered as one of the simplest methods for measuring the real and imaginary parts of the complex nonlinear refractive index of materials. Despite its simplicity, in many cases, the original z-scan theory [12] is not completely accurate, i.e. when the nonlinear medium response to laser radiation is nonlocal in space. Whenever the laser induced nonlinear response at a certain point of the medium is not solely determined by the laser intensity at that point, but also depends on the laser intensity in the surrounding regions, it will be called a nonlocal nonlinear optical response [13]. Generally, a variety of mechanisms may contribute to the nonlinearity, some of which may be nonlocal [14]. For instance, when the nonlinear medium is dispersed inside a dielectric solution, reorientation of the dipoles (permanent or induced molecular dipoles) as a result of the optical field action is nonlocal in space and changes the electric field experienced by the nonlinear medium. Recently, the z-scan theory has been generalized to consider the possibility of the sample nonlocal response in case of pure nonlinear refraction [15] and nonlinear refraction at the presence of nonlinear absorption [16]. It is shown that nanostructures can exhibit nonlocal responses due to the laser beam scattering by nanoparticles [17]. However, a variety of other mechanisms may produce the nonlocal nonlinear response of nanostructures, such as the dipolar response of the induced or permanent polarized molecules of the material that contains the nano-objects. The nonlocal z-scan theory [15,16], can be used for systematically analyzing the role of various mechanisms in producing the nonlocal nonlinear response of different materials.

Recently, we have reported a new method for synthesizing GO supported Au nanoparticles [18]. In this paper, we describe the preparation of GO/Au dispersions in three different solvents, i.e. water, DMF (N,N-Dimethylformamide) and NMP (N-Methyl-2-pyrrolidone). Nonlinear optical properties of the resultant dispersions have been measured using the z-scan technique. The nonlocal z-scan theory [16] has been used for analyzing the measured data and to obtain the nonlinear refractive index, nonlinear absorption coefficient and order of nonlocality of the dispersions.

2. Experimental Part

Preparation of Au nanoparticles and synthesis of GO and GO/Au powders was explained in our previous work in detail [18]. Preparation of GO/Au suspensions in different solvents will be described. The method of measuring the nonlinear optical properties of materials will be explained thereafter.

The GO/Au suspensions were prepared in three different solvents: water, DMF (N,N-Dimethylformamide) and NMP (N-Methyl-2-pyrrolidone) with a concentration of 2 mg/mL. The dispersions in each solvent were prepared by a 1 h sonication. The dispersions were further centrifuged at 5000 rpm for 20 min. GO suspensions were also prepared in the three mentioned solvents without the Au nanoparticles to study the role of nanoparticles addition on their optical properties.

The z-scan technique was used for measuring the complex nonlinear indices of refractions of the GO/Au suspensions. Scheme of the used z-scan experimental setup is shown in Fig. (1).

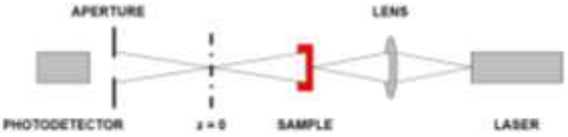

Fig. (1) Schematic illustration of the z-scan setup

In this setup, the laser beam (CW He-Cd, λ=442nm, P= 12 mW) is focused to a spot size of 1.6 μm by an f= 25 cm convex lens. The beam spot size is first measured on the focusing lens by a CCD camera (SAMSUNG SDC415PH) and then calculated at the focal position using the well-known thin lens conversion formulas [19]. In order to avoid the CCD saturation or damage, the laser beam intensity is reduced by a variable beam attenuator consisting of a half-wave plate and a polarizing beam splitter cube. A 1 mm thickness quartz cell containing the suspension is moved along the optical axis (the z axis) from one to the other side of the lens focal point. Before measurements, suspensions were ultrasonicated for 20 minutes to prevent their precipitation. For measuring the real part of the nonlinear refractive index, the z-scan setup is used in its closed-aperture form which is shown in Fig. (1). In this form, since the nonlinear material reacts like a weak z-dependent lens [20], the far-field aperture makes it possible to detect the small beam distortions in the original beam. Since the focusing power of this weak nonlinear lens depends on the nonlinear refractive index [20], it would be possible to extract its value by analyzing the z-dependent data acquired by the detector and by cautiously interpreting them using an appropriate theory [16]. To measure the imaginary part of the nonlinear refractive index, or the nonlinear absorption coefficient, the z-scan setup is used in its open-aperture form. In open-aperture measurements, the far-field aperture is removed and the whole signal is measured by the detector. By measuring the whole signal, the beam small distortions become insignificant and the z-dependent signal variation is due to the nonlinear absorption entirely. Using the z-scan theory [12,16], one can find the value of the nonlinear absorption coefficient.

3. Results and Discussion

The resulting solution of Au-NPs was characterized by UV-Visible spectroscopy. Figure (2) shows the UV-Vis absorption spectrum of Au nanoparticles solution. In this work, All the UV-Visible measurements were performed at room temperature by a Perkin Elmer 550ES from 300 to 750 nm with a resolution of 1 nm. The resonance at 531 nm is clearly seen and arises due to the excitation of surface plasmon vibrations in the Au nanoparticles [21]. The presence of this plasmonic absorption peak is clear evidence in support of the formation of Au nanoparticles.

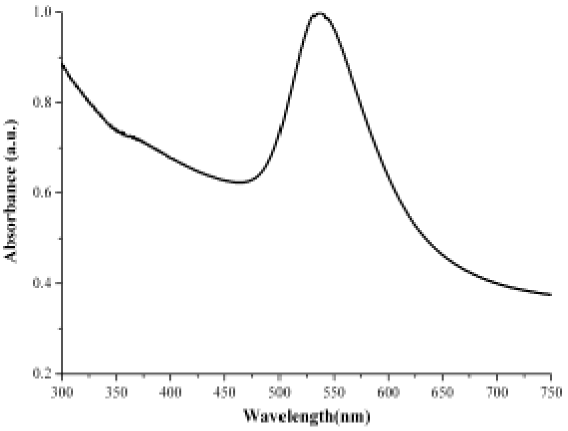

Fig. (2) Absorption spectrum of Au nanoparticles solution

In Fig. (3), the Transmission Electron Microscopy (TEM) image of the Au nanoparticles is shown. TEM images were taken by Philips CM120 transmission electron microscope. The estimated mean particle size of Au nanoparticles is about 27 nm. The mean particle size was obtained by measuring the diameter of over 100 particles in all the TEM images to ensure good statistics.

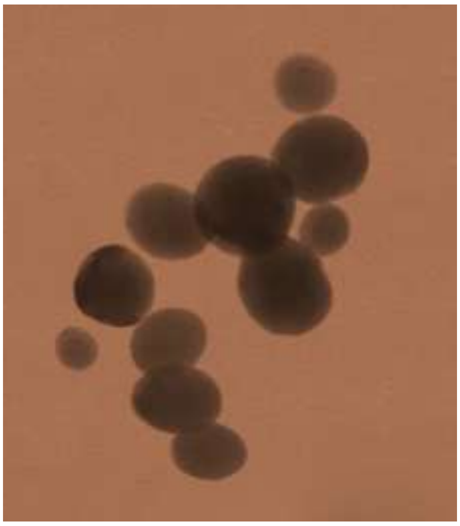

Fig. (3) TEM image of Au nanoparticles

Figure (4) shows the TEM images of GO/Au nanocomposite powder. It can be seen that Au nanoparticles are distributed between the GO layers.

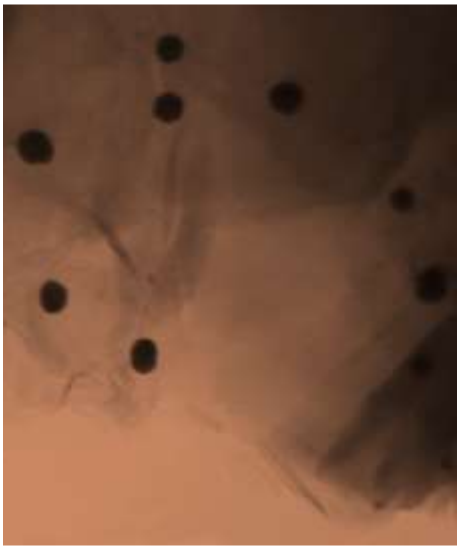

Fig. (4) TEM image of GO/Au nanocomposite powder

Figure (5) shows the optical absorption spectra of the GO suspensions in three solvents with and without the presence of Au nanoparticles. For simplicity, we have named GO suspensions in DMF (N,N-Dimethylformamide), water and NMP (N-Methyl-2-pyrrolidone) as the G-D, G-W and G-N, respectively. Furthermore, GO/Au suspensions in DMF, water and NMP are also respectively named as G-A-D, G-A-W and G-A-N. It can be seen that by addition of Au nanoparticles to G-D, G-W and G-N, Au plasmonic absorption peak appears on the G-A-D, G-A-W and G-A-N absorption spectra. The plasmonic absorption peak of the Au nanoparticles at 531 nm is a little red-shifted in DMF and shifted more toward the blue end of the visible spectrum by changing their surrounding medium from water to NMP. In order to more clearly see these features, the measured wavelengths at which plasmonic resonances have occurred are listed in table (1).

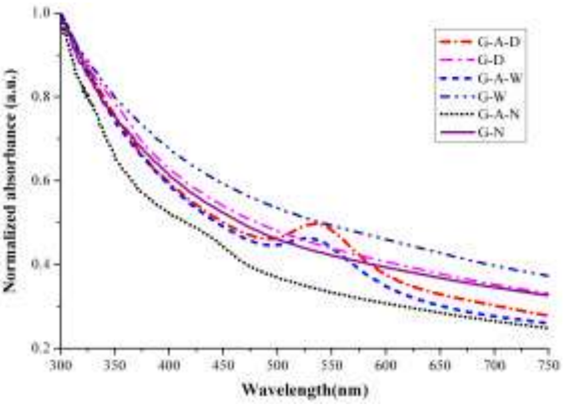

Fig. (5) Optical absorption spectra of GO and GO/Au dispersions in different solvents. Acronyms: G-A-D (GO/Au in DMF), G-D (GO in DMF), G-A-W (GO/Au in water), G-W (GO in water), G-A-N (GO/Au in NMP) and G-N (GO in NMP)

Inspecting Fig. (5), one can also see that the plasmonic peak is less predominant in NMP solution. Since G-A-D, G-A-W and G-A-N have GO/Au in common, variation of their linear optical properties can be attributed to their different solvents that surround the Au nanoparticles. Indeed, according to the Mie theory, the wavelength at which plasmon resonance occurs depends on optical characteristics of the medium which surrounds the nanoparticles [22]. It would be of no surprise if the surrounding medium can also play an influential role in determining the nonlinear optical response of nanoparticles.

If the surrounding medium has a dielectric nature, it can change the induced nonlinear phase shift in the impinging laser beam on the sample surface in z-scan experiments due to its nonlocal action [14,15].

The complex nonlinear refractive index of all the specimens was measured using the z-scan technique. To this end, z-scan technique was used in both closed and open aperture configurations. For G-D, G-W, G-N and Au nanoparticles suspensions, no detectable signal could be detected by the far-field detector which means that these samples do not produce a detectable nonlinear response for the used experimental conditions. Indeed, in the first order of approximation, the intensity dependent nonlinear refractive index and absorption coefficient can be written as:

$$n = n_0 + n_2 I \quad (1)$$

$$\alpha = \alpha_0 + \beta I \quad (2)$$

where n_0 and α_0 and n_2 and β are the linear refractive index and absorption coefficient and nonlinear refractive index and absorption coefficient, respectively. Since the intensity itself is proportional to the laser power, we have chosen the laser power as low as possible (12 mW) to be able to study the sole effect of Au nanoparticles addition to G-D, G-W and G-N. Indeed, these samples had nonlinear responses for higher laser powers. We have deliberately decreased the laser power to a level that no detectable signal could be measured for these samples. This would make the final conclusions more obvious and one can easily evaluate the role of Au nanoparticles addition in changing the nonlinear responses of G-D, G-W and G-N. Furthermore, if the exciting laser source has a wavelength (i.e., 442 nm in our case) far from the surface plasmonic absorption peak of nanoparticles (537 nm for Au nanoparticles), one can avoid the plasmonic resonance contribution in the nonlinear response of the samples. This would also reduce the thermal effect contribution in the nonlocal response of the samples and make it possible to concentrate on the role of the dielectric nature of the solvents itself.

Table (1) The measured plasmonic absorption peak wavelengths of Au nanoparticles suspension as well as GO/Au dispersions in deferent solvents

Absorption Peak (nm)			
Au	G-A-D	G-A-W	G-A-N
537	534	527	435

The open aperture z-scan data of G-A-D, G-A-N and G-A-W are represented in figures 6(a-c). Furthermore. The reverse saturable absorption behavior in Fig. (6) are shown to be characteristics of the GO [6,7,23]. The nonlocal z-scan theory [16] is used for finding the nonlinear refractive index and nonlinear absorption coefficient of the samples. In short, in this theory the nonlinear absorption coefficient and refractive index can be found using a two-step procedure. Using the open aperture z-scan data, the nonlinear absorption coefficient β can be deduced by performing a one parameter fit using the following equation:

$$T_o(z) = \frac{\ln\left(1 + q_0(z)\right)}{q_0(z)} \tag{3}$$

with

$$q_0(z) = \frac{\beta I_0 L_{\text{eff}}}{1 + (z/z_0)^2} \tag{4}$$

where $L_{\text{eff}} = (1 - \exp(-\alpha_0 L))/\alpha_0$ is the sample effective thickness and is defined using the sample real thickness L. I_0 being the on-axis intensity at focus and z_0 is the laser beam Rayleigh length. In the second step and with β known, the nonlinear index of refraction n_2 and the nonlinear parameter m can be obtained with a two parameter fit on the closed-aperture z-scan data using the next equation:

$$T_c(z) = 1 - \frac{\left(4mkn_2 x + \beta\left(x^2 + (2m+1)\right)\right) I_0 L_{\text{eff}}}{(x^2 + (2m+1)^2)(x^2+1)} \tag{5}$$

where $x=z/z_0$ and k is the wave number. The nonlinear least squares fitting is used to fit Eq. (5) to the measured closed aperture z-scan data. The trust-region algorithm of the MATLAB software is implemented for this purpose. The phenomenological parameter m is the order of nonlocality and can be any real positive number. This parameter shows the nonlocality amount in the sample response to the electric field of the irradiating laser beam [15,16].

In this study, the dipolar response of the induced or permanent polarized molecules of the materials that surround the Au nanoparticles can produce the nonlocality. Since all the samples have GO in common, their different nonlocal responses can be attributed to their different kinds of solvents. The fitting results according to equations (3) and (5) are also respectively shown by solid lines in Fig. (6). The measured nonlinear optical properties of the samples are summarized in table (2). G-A-N exhibits superior nonlinear optical properties in comparison with G-A-D and G-A-W.

Note that although the linear absorption coefficient of G-A-N is less than 2 times than that of the G-A-D, the nonlinear refraction of the former is around 200 times larger than the latter. We are of the opinion that the different nonlocal responses of their corresponding solvents, NMP in the former and DMF in the latter, is the major reason for this difference. One must note that nonlinear scattering by Au nanoparticles and heat distribution or the thermal effect may also contribute in the nonlocal response of the samples. However, two points seem in order. First, all the samples have been prepared in the same way and we expect nearly equal amounts of Au nanoparticles in the same volumes of them. Therefore, it is also expected that Au nanopaticles contribution in the observed nonlocality, be nearly the same for all the samples. Second, since the linear absorption coefficients of the samples have the same order of magnitudes (see table 2), and this coefficient mainly determines the amount of deposited heat inside the samples, we expect the amount of nonlocality due to the resulted temperature gradient be also at the same order of magnitudes for all of them. Therefore, one can conclude that this is the dielectric nature of the surrounding media that dominates the nonlocality and results in the considerable difference between the nonlinear responses of G-A-D, G-A-N and G-A-W. Unfortunately, the nonlocal z-scan theory [15,16] is unable to distinguish between the various nonlocal mechanisms in z-scan experiments in its current form, and more work should be done to further develop it.

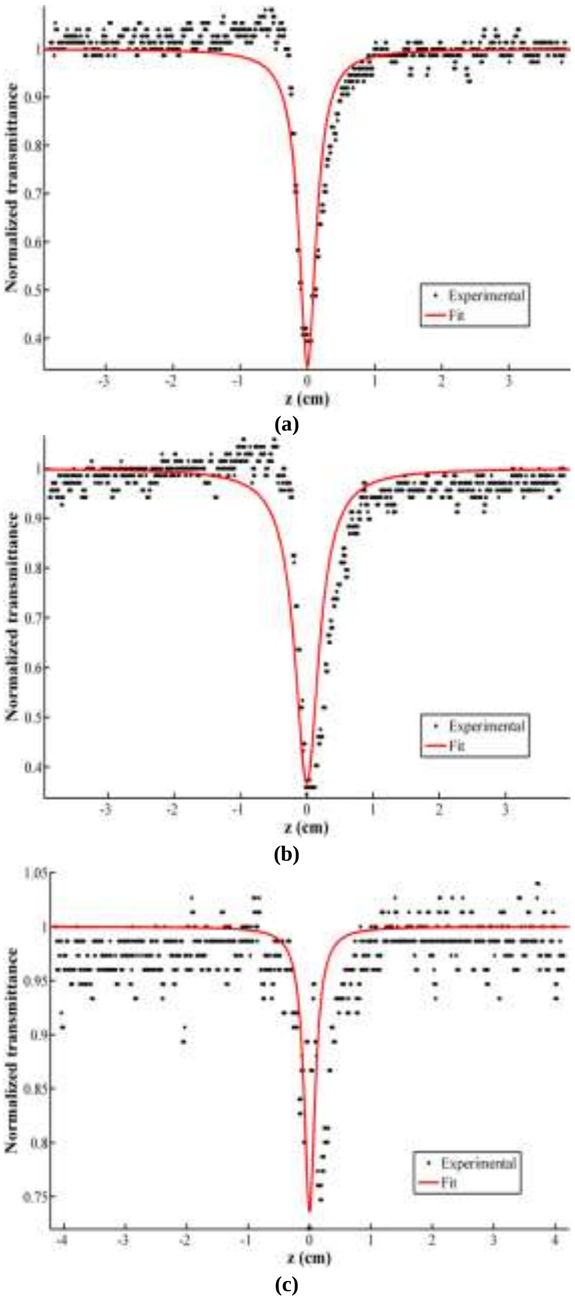

Fig. (6) Open aperture z-scan data (dots) and fitting results (solid lines) of a) G-A-D, b) G-A-N and c) G-A-W. All the three samples exhibit reverse saturable absorption for the used laser wavelength

The most noteworthy point about table (2) is that the nonlocal parameter of G-A-N is relatively larger than those of the G-A-D and G-A-W. This may indicates the more polarizability of the G-A-N compared with G-A-N and G-A-W. Since *m* is a phenomenological parameter and is included in the sample nonlinear response just for considering the difference between the spatial distribution of the induced nonlinear phase shift and the laser beam intensity distribution [15], much more studies are needed to approve this conclusion. Indeed, the nonlocal z-scan theory should be further developed to quantify the role of various physical phenomena that may change the sample nonlinear response. Another important point that should be noted is that by addition of Au nanoparticles, the nonlinear optical properties of GO in different solvents have been improved considerably. The enhanced nonlinear optical behaviors may arise due to the enhanced nonlinear scattering by the incorporated Au nanoparticles. Indeed, as we have pointed out previously, nonlocality arises when the laser induced nonlinear response at a certain point of the medium depends also on the laser intensity in the surrounding regions. The nonlinear scattering of Au nanoparticles, which depends on the laser intensity at their positions, can change the nonlinear response at other positions and hence can contribute in the nonlocal response of the media. The improved nonlinear optical properties of GO can broaden its application in various fields. Its larger nonlinear refractive index can find a possible application in optical switches and its enhanced reverse saturable absorption, which can be seen in figure 6, can bring it into application in optical limiters.

Table (2) Nonlinear optical properties of G-A-D, G-A-N and G-A-W. The linear optical absorption coefficients at 442 nm are also given in the last column

sample	n_2 (cm^2/W)	β (cm/W)	m	α (cm^{-1})
G-A-D	2.3×10^{-7}	4.4×10^{-3}	5.2	1.31
G-A-N	4.5×10^{-5}	6.2×10^{-3}	422	2.16
G-A-W	6.2×10^{-12}	1.2×10^{-3}	1.4	1.09

4. Conclusion

GO, Au nanoparticles and GO/Au nanodispersions in different solvents have been prepared and their optical, structural and nonlinear optical properties have been studied in this work. It is shown that the solvent material can change the optical and nonlinear optical properties of GO/Au. It is proposed that the nonlocal action of the solvent material may be the source of variation of the nonlinear optical properties of the samples. This proposal is confirmed by applying the nonlocal z-scan theory [15,16] for analyzing the z-scan measurement data. Previously, it was also shown that the light scattering by nanoparticles may be the source of nonlocality in the sample response in z-scan measurements [17]. We are of the opinion that whenever one expects the sample nonlocal response in z-scan experiments, the nonlocal z-scan theory should be used to measure the more accurate values of the nonlinear refractive and absorption coefficients. More future studies can be conducted to examine the role of other nonlocal mechanisms in z-scan experiments. The nonlocal z-scan theory should also be further developed to for quantifying the role of various nonlocal mechanisms. In this way, it would be possible to extract the values of other constants, like the sample polarizability or heat diffusion coefficient, from the measured nonlocal parameter.

It is also shown that the incorporation of Au nanoparticles can enhance the nonlinear optical behavior of the GO. The improved nonlinear optical properties of GO can open new avenues for its application in various fields. Other metallic nanoparticles may also improve the nonlinear optical properties of the GO and many more experiments can be performed to investigate how they can do this. Such works are in progress and will be reported in near future.

References

[1] Tutt L W and Kost A 1992 Optical limiting performance of C60 and C70 solution *Nature* **356** 225–226.

[2] Couris S, Koudoumas E, Ruth A A and Leach S 1995 Concentration and wavelength dependence of the effective third-order susceptibility and optical limiting of C60 in toluene solution *J. Phys. B: Atom. Mol. Opt. Phys.* **28** 4537.

[3] Hasan T et al. Nanotube–Polymer Composites for Ultrafast Photonics 2009 *Adv. Mater.* **21** 3874–99.

[4] Bonaccorso F, Sun Z, Hasan T and Ferrari A C 2010 Graphene photonics and optoelectronics *Nat. Photon.* **4** (9) 611–22.

[5] Hendry E, Hale P J, Moger J and Savchenko A K 2010 Coherent nonlinear optical response of grapheme *Phys. Rev. Lett.* **105** 097401-04.

[6] Yamuna R, Ramakrishnan S, Dhara K, Devi R, Kothurkar N K, Kirubha E and Palanisamy P K 2013 Synthesis, characterization, and nonlinear optical properties of graphene oxide functionalized with tetra-amino porphyrin *J. Nanopart. Res.* **15** 1-9.

[7] Liaros N, Iliopoulos K, Stylianakis M M, Koudoumas E and Couris S 2014 Optical limiting action of few layered graphene oxide dispersed in different solvents *Opt. Mater.* **36** 112–17.

[8] He T, Qi X, Chen R, Wei J, Zhang H and Sun H 2012 Enhanced optical nonlinearity in noncovalently functionalized amphiphilic graphene composites *ChemPlusChem* **77**(8), 688-93.

[9] He T, Wei W, Ma L, Chen R, Wu S, Zhang H, Sun H 2012 Mechanism studies on the superior optical limiting observed in graphene oxide covalently functionalized with upconversion $NaYF_4$: Yb^{3+}/Er^{3+} nanoparticles *small* **8**(14), 2163-68.

[10] Zhang X L, Liu Z B, Yan X Q, Li X C, Chen Y S and Tian J G 2015 Nonlinear optical and optical limiting properties of fullerene, multi-walled carbon nanotubes, graphene and their derivatives with oxygen-containing functional groups *J. Opt.* **17**(1), 015501.

[11] Sheik-Bahae M, Said A A and Van Stryland E W 1989 High-sensitivity single-beam n_2 measurements *Opt. Lett.* **14** 955–57.

[12] Sheik-Bahae M, Said A A, Wei T H, Hagan D J and Van Stryland E W 1990 Sensitive measurement of optical nonlinearities using a single beam *IEEE J. Quantum Electron.* **26** 760–769.

[13] Krolikowski W, Bang O, Nikolov N I, Neshev D, Wyller J, Rasmussen J J and Edmundson D 2004 Modulational instability, solitons and beam propagation in spatially nonlocal nonlinear media *Journal of optics B: quantum and semiclassical optics* **6**(5), S288.

[14] Cuppo F, FigueiredoNeto A M, Gomez S and Palffy-Muhoray P 2002 Thermal-lens model compared with the Sheik-Bahae formalism in interpreting Z-scan experiments on lyotropic liquid crystals *J. Opt. Soc. Am. B* **19**, 1342-48.

[15] Rashidian Vaziri M R, Hajiesmaeilbaigi F and Maleki M H 2013 Generalizing the Z-scan theory for nonlocal nonlinear media *J. Opt.* **15** 025201.

[16] Rashidian Vaziri M R 2013 Z-scan theory for nonlocal nonlinear media with simultaneous nonlinear refraction and nonlinear absorption *Appl. Opt.* **52**, 4843.

[17] Farmanfarmaei B, RashidianVaziri M R and Hajiesmaeilbaigi F 2014 Investigation of the nonlocal nonlinear optical response of copper nanostructured thin films prepared by pulsed laser deposition *Quantum Electron.* **44** (11) 1029–32.

[18] Fakhri P, Nasrollahzadeh M and Jaleh B 2014 Graphene oxide supported Au nanoparticles as an efficient catalyst for reduction of nitro compounds and Suzuki–Miyaura coupling in water *RSC Adv.* **4** 48691.

[19] Saleh B E A and Teich M C 2007 *Fundamentals of Photonics* 2nd edn (New York: Wiley) pp 86-89.

[20] Rashidian Vaziri M R 2014 Comment on Nonlinear refraction measurements of materials using the moiré deflectometry *Opt. Commun.* In Press doi:10.1016/j.optcom.2014.09.017.

[21] Xu X H N, Huang S, Brownlow W, Salaita K and Jeffers R B 2004 Size and Temperature Dependence of Surface Plasmon Absorption of Gold Nanoparticles Induced by Tris(2,2‘-bipyridine)ruthenium(II) *J. Phys. Chem. B* **108** (40) 15543–51.

[22] Kreibig U and Völlmer M 1995 *Optical Properties of Metal Clusters* (Berlin: Springer).

**THE IRAQI JOURNAL OF
APPLIED PHYSICS**
EDITORIAL BOARD

COPYRIGHT RELEASE FORM
IRAQI JOURNAL OF APPLIED PHYSICS (IJAP)

We, the undersigned, the author/authors of the article titled
……
……
……
……
……
……
……

that is submitted to the Iraqi Journal of Applied Physics (IJAP) for publication, declare that we have neither taken part or full text from any published work by others, nor presented or published it elsewhere in any other journal. We also declare transferring copyrights and conduct of this article to the Iraqi Journal of Applied Physics (IJAP) after accepting it for publication.

The authors will keep the following rights:

1. Possession of the article such as patent rights.
2. Free of charge use of the article or part of it in any future work by the authors such as books and lecture notes after informing IJAP editorial board.
3. Republishing the article for any personal purposes of the authors after taking journal permission.

To be signed by all authors:

Signature:……………………………………………………..…..date: ………………………….………………
Printed name: ……………………………………………………………………………………………………

Signature:……………………………………………………..…..date: ………………………….………………
Printed name: ……………………………………………………………………………………………………

Signature:……………………………………………………..…..date: ………………………….………………
Printed name: ……………………………………………………………………………………………………

Correspondence
address:…………………..……………..………………………………………………………………..
……
Address:……………………………………………..……………………………………………………
……
Telephone:…………………….…..………………….email: …………………………………………………

Note: Complete and sign this form and mail it to the below address with your finally revised manuscript

The Iraqi Journal of Applied Physics
www.iraqiphysicsjournal.com
Email: info@iraqiphysicsjournal.com
Email: editor_ijap@yahoo.co.uk
Email: irq_appl_phys@yahoo.com

IRAQI JOURNAL OF APPLIED PHYSICS

Volume (17), Issue (1), January-March 2021

CONTENTS